ARTICLES
https://doi.org/10.1038/s41592-020-0913-x

nature methods

Check for updates

Rational design and implementation of a chemically inducible heterotrimerization system

Helen D. Wu[1,2], Masaki Kikuchi[3], Onur Dagliyan[4], Adam K. Aragaki[2,5], Hideki Nakamura[2,8], Nikolay V. Dokholyan[6,7], Takashi Umehara[3]✉ and Takanari Inoue[1,2,5]✉

Chemically inducible dimerization (CID) uses a small molecule to induce binding of two different proteins. CID tools such as the FK506-binding protein–FKBP–rapamycin-binding– (FKBP–FRB)–rapamycin system have been widely used to probe molecular events inside and outside cells. While various CID tools are available, chemically inducible trimerization (CIT) does not exist, due to inherent challenges in designing a chemical that simultaneously binds three proteins with high affinity and specificity. Here, we developed CIT by rationally splitting FRB and FKBP. Cellular and structural datasets showed efficient trimerization of split pairs of FRB or FKBP with full-length FKBP or FRB, respectively, by rapamycin. CIT rapidly induced tri-organellar junctions and perturbed intended membrane lipids exclusively at select membrane contact sites. By conferring one additional condition to what is achievable with CID, CIT expands the types of manipulation in single live cells to address cell biology questions otherwise intractable and engineer cell functions for future synthetic biology applications.

Chemically inducible dimerization (CID) uses a bifunctional small molecule to bring together two proteins with high affinity, specificity and fast kinetics[1,2]. CID systems such as the rapamycin-dependent FKBP–FRB heterodimerization (Fig. 1a) exert tight spatiotemporal control over local protein concentrations by oligomerization[3] or by rapidly translocating a protein of interest to or from a desired site of action[4,5]. Such strategies have enabled signal parsing of a given protein from the noise of other cell signaling pathways, leading to discoveries in cell migration, endocytosis, transcription and translation[1,2,6]. The seconds-to-minutes timescale offers a further advantage: CID strategies are less susceptible to genetic compensation that sometimes plague knockdown or knockout methods. When used as a building block for rewiring circuits in a bottom-up approach, CID systems have created fast, translation-independent synthetic logic gates in mammalian cells[7]. Over the years, CID has become a widely used, easily generalizable chemical biology tool with promising clinical impact[8].

While there have been hundreds of applications of CID, no rapidly inducible trimerization system has been developed to our knowledge. While the concept of trimerization has been demonstrated previously, for instance, with guide RNA as a trigger to trimerization of split Cas9 proteins and a specific DNA site[9], we sought to develop a tool with modularity and broad applicability. Indeed, examples of transient or stable trimerization in biology exist, including but not limited to trimeric G proteins[10], inner ear epithelial cell junctions[11] and MHC–antigen–TCR complexes governing T cell selection[12]. Engineering chemically inducible trimerization (CIT) could address biologically relevant questions, and expand what is achievable with chemical biology.

In theory, CIT should comprise three unique protein components that can be brought together by a tri-functional small molecule. However, trimerization is difficult to achieve, as recruiting an additional protein doubles the possible bound states of the small molecule compared to dimerization (Supplementary Fig. 1). Efficient trimerization requires that the trimeric complex be the most favorable state over other less bound configurations. For efficient CID, positive cooperativity is essential: once a CID protein binds rapamycin, the resulting rapamycin–protein complex binds the second protein with more than 1,000-fold higher affinity than rapamycin alone[13]. This unique cooperativity is mediated through electrostatic interactions at the FKBP–rapamcycin–FRB interface[14]. Because engineering de novo proteins with appropriate small molecule-dependent surface interactions should be highly challenging, we instead exploited the special properties of the FKBP–FRB–CID system to achieve trimerization.

We present a CIT system whose components comprise split FRB and FKBP proteins (Fig. 1a). Candidate split proteins were computationally determined and characterized for their efficacy of trimerization in cells. Formation of the trimer in vitro was assessed by X-ray crystallography. CIT was used to target cytosolic proteins to inter-organelle membrane junctions and induce tri-organellar endoplasic reticulum–plasma-membrane– (ER–PM)–mitochondria contacts. Finally, we used CIT to locally alter phosphoinositide composition of ER–PM junctions. Altogether, CIT has small components that trimerize with fast kinetics in a rapamycin-inducible manner, expanding the variety of perturbations possible in the chemical biology toolkit.

Results

Design of split FRB and FKBP. We determined FRB and FKBP candidate split sites through rational design. We selected FRB (human mammalian target of rapamycin (mTOR) residues 2021–2113)

[1]Department of Biomedical Engineering, Johns Hopkins University School of Medicine, Baltimore, MD, USA. [2]Department of Cell Biology, Center for Cell Dynamics, Johns Hopkins University School of Medicine, Baltimore, MD, USA. [3]Laboratory for Epigenetics Drug Discovery, RIKEN Center for Biosystems Dynamics Research, Yokohama, Kanagawa, Japan. [4]Department of Neurobiology, Harvard Medical School, Boston, MA, USA. [5]Department of Pharmacology, Johns Hopkins University School of Medicine, Baltimore, MD, USA. [6]Departments of Pharmacology and Biochemistry & Molecular Biology, Penn State University College of Medicine, Hershey, PA, USA. [7]Departments of Chemistry and Biomedical Engineering, Pennsylvania State University, University Park, PA, USA. [8]Present address: Kyoto University Graduate School of Engineering, Department of Synthetic Chemistry and Biological Chemistry, Katsura Int'tech Center, Graduate School of Engineering, Kyoto University, Nishikyo-ku, Kyoto, Japan. ✉e-mail: takashi.umehara@riken.jp; jctinoue@jhmi.edu

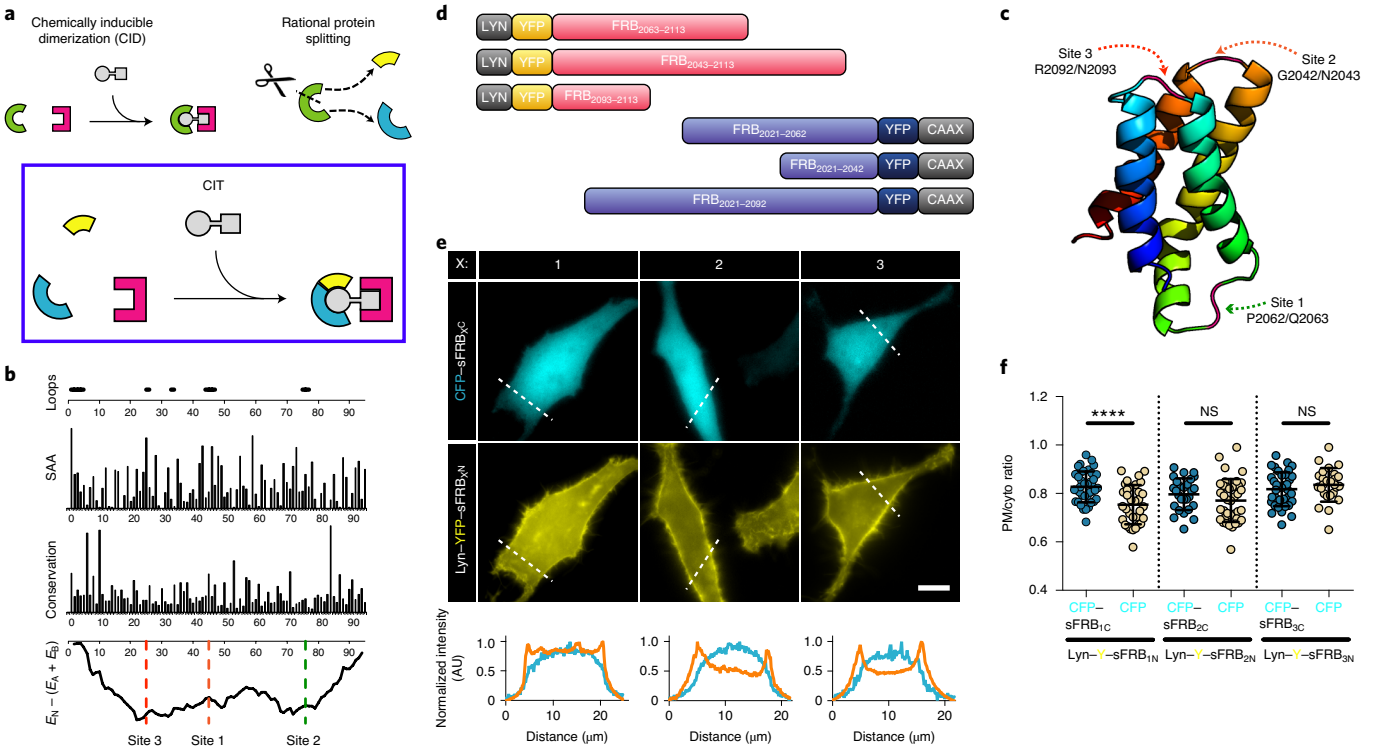

Fig. 1 | Rational CIT design and sFRB overexpression in cells. a, CID protein FRB (green arc) sites generate FRB protein halves (yellow and blue). Split FRB halves and FKBP form three components of CIT. Rapamycin brings them together. **b**, Computational analysis to determine split sites for FRB domain only. Loop areas with high solvent accessibility area (SAA), low conservation and favorable split energy profiles were chosen. E_N is the energy of the native structure, while E_A and E_B are the energies of the respective split parts, calculated using the MEDUSA scoring function. **c**, FRB structure (PDB ID 1AUE) consists of four α-helices; split sites 1, 2 and 3 all reside in linker regions between α-helices. **d**, Examples of sFRB fusion protein design. Lyn or CAAX motifs target sFRBs to the PM. **e**, Co-overexpression of sFRB protein pairs in HeLa cells. N-terminal sFRB halves (sFRB$_{1N}$, sFRB$_{2N}$, sFRB$_{3N}$) are PM localized by Lyn and C-terminal sFRB halves (sFRB$_{1C}$, sFRB$_{2C}$, sFRB$_{3C}$) are cytosolic. Line scans below show normalized PM (orange) and cytosolic (blue) signal intensity. **f**, Pre-association between sFRB halves. PM-to-cytosolic ratios derived from line scans of cytosolic sFRB$_{1C}$, sFRB$_{2C}$ and sFRB$_{3C}$ coexpressed with PM-targeted sFRB$_{1N}$, sFRB$_{2N}$ and sFRB$_{3N}$, respectively, compared to CFP alone. Data are presented as mean values ± s.d. From left to right: 39, 33, 27, 39, 36 and 26 cells; three independent experiments each. Two-tailed Student's *t*-test assuming equal variance was used. ****$P < 0.0001$; NS, not significant. Scale bar, 10 μm.

with a T2098L mutation, which makes it otherwise unstable unless bound to chemical ligands or FKBP[15], to decrease recombination potential after protein splitting (Fig. 1b). FRB T2098L can also recognize rapamycin analog AP21967, which unlike rapamycin does not bind mTOR pathways, and could be used in in vivo biological studies without toxicity[16,17]. In splitting FRB, we avoided its four alpha helices, crucial residues for FRB–FKBP–rapamycin stabilization (L2031, S2035, Y2038, F2039, T2098L, W2101, D2102 and Y2105)[14] and regions of high conservation in the three FRB loops (Fig. 1c and Supplementary Fig. 2a,b). The SPELL algorithm[18] was used to pinpoint candidate split sites in FRB through computational analysis. All loops selected for splitting (Fig. 1b,c and Supplementary Fig. 2a) show low evolutionary conservation with Kullback–Leibler conservation scores <2 and have solvent accessible area values >30 Å^2 (Fig. 1b)[18–20]. The split energy profile determined by computing energy of the split parts relative to native energy of the intact protein (Fig. 1b) shows the three FRB loops residing in two major energy wells, which indicate FRB halves split at these sites are less likely to pre-associate[18]. Split sites for FKBP were also determined in this manner (Supplementary Fig. 4a,b). Hereafter, split FRB or FKBP proteins are abbreviated to sFRB or sFKBP. Each split site is numbered in terms of likelihood of success based on computational analysis; sFRB$_1$, sFRB$_2$ and sFRB$_3$ refer to pairs of sFRB proteins split at sites 1, 2 or 3, with split site 1 most likely to succeed. The N- or C-terminal half of a given sFRB protein pair is sFRBχ_N or sFRBχ_C, χ being the split site number.

We generated plasmids of N-terminal fluorophore-tagged-sFRB proteins and observed cytosolic expression in transfected HeLa cells (Supplementary Fig. 2c). We also generated Lyn or CAAX-tagged-sFRB fusion proteins, all of which correctly localized to the PM (Fig. 1d). To determine the extent of possible pre-association between sFRB pairs, we used the Lyn motif to target sFRBχ_N to the PM, and observed the localization of corresponding cytosolic sFRBχ_C across all three split sites ($\chi = 1, 2, 3$). Higher PM-to-cytosol ratios occurred between Lyn–Y–sFRB$_{1N}$ and CFP (cyan fluorescent protein)–sFRB$_{1C}$ compared to Lyn–Y–sFRB$_{1N}$ and CFP alone (Fig. 1e,f, 0.83 ± 0.01 versus 0.75 ± 0.01, $P < 0.0001$). In contrast, cytosolic CFP–sFRB$_{2N}$ and sFRB$_{3N}$ PM-to-cytosol ratios did not differ from CFP alone (0.80 ± 0.01 versus 0.77 ± 0.01, 0.82 ± 0.01 versus 0.84 ± 0.01, respectively), suggesting the sFRB$_1$ pair has higher tendency to pre-associate. This approach to designing split sites, validating cytosolic protein expression and generating membrane-anchored protein was also applied to sFKBP.

Characterization of split FRB. The sFRB protein pairs were tested for their ability to bind FKBP in a rapamycin-inducible manner to achieve CIT. We coexpressed cytosolic FKBP with PM-localized sFRB pairs in HeLa cells. If functional, rapamycin would shift FKBP localization from the cytosol to the PM (Fig. 2a). sFRB pairs were localized to the PM with Lyn and CAAX tags (Fig. 1d). On rapamycin addition, all three sFRB pairs recruited mCh–FKBP to the PM, comparable to full-length (FL) FRB (Fig. 2b). Changes in cell line

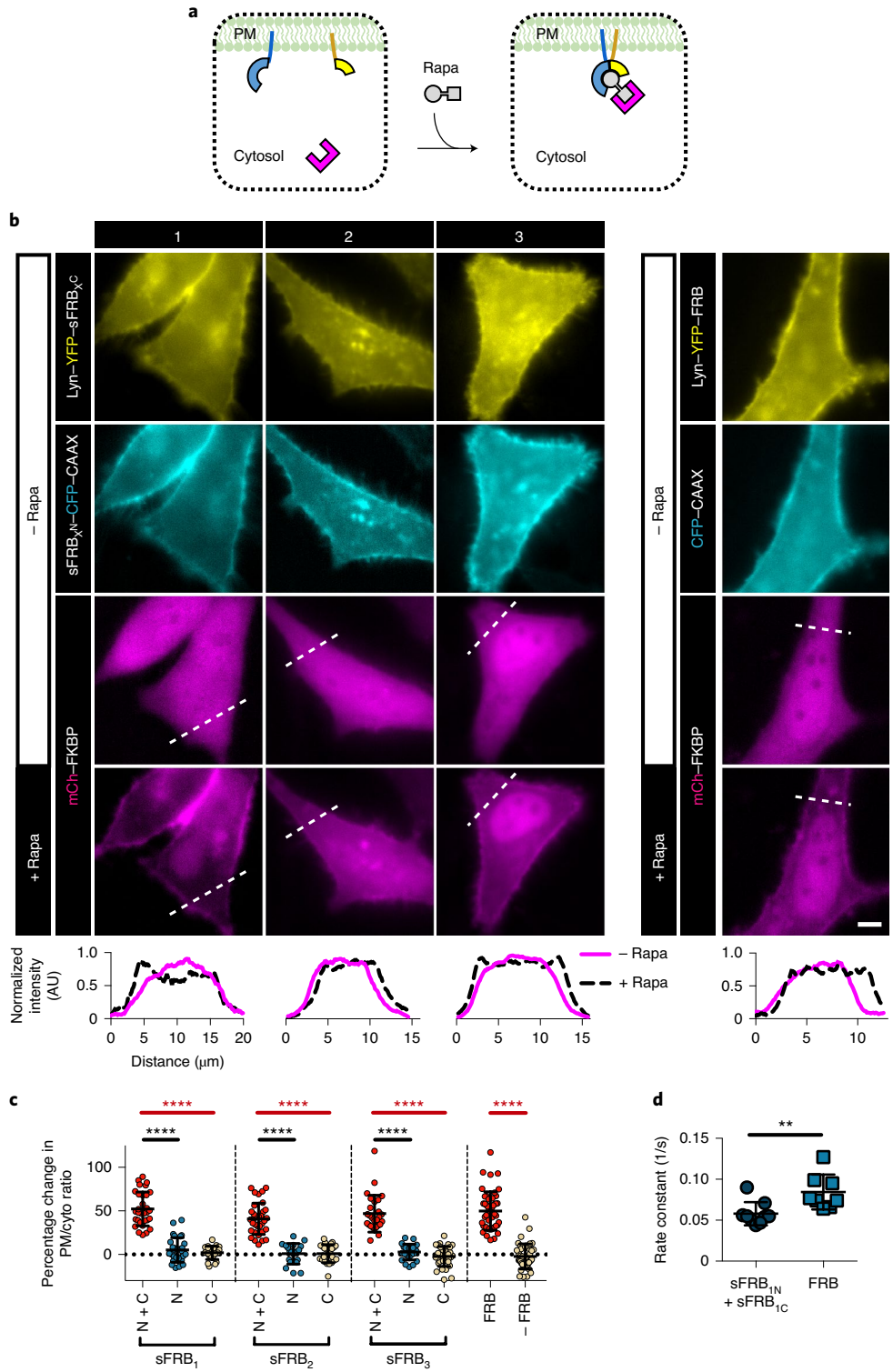

Fig. 2 | Characterization of FKBP recruitment extent and kinetics by sFRB after rapamycin addition. a, Experimental setup for FKBP recruitment efficacy by sFRBs. sFRB N- and C-terminal halves are PM-targeted by CAAX or Lyn, respectively, and coexpressed with FKBP. Cytosol to PM translocation by FKBP indicates successful recruitment. **b**, Translocation of FKBP from cytosol to PM in HeLa cells coexpressing PM-targeted sFRB$_1$, sFRB$_2$, sFRB$_3$ pairs and full-length FRB. Before rapamycin, top three rows; 9 min after rapamycin, bottom row. Line scans show corresponding normalized intensity of mCh–FKBP signal. **c**, Percentage change in mCh–FKBP PM-to-cytosolic ratio before and after rapamycin addition. FKBP recruitment by sFRB pairs (N + C) compared to N- or C-terminal halves only (N or C), full-length FRB or no FRB in FKBP recruitment. Data are presented as mean values ± s.d. From left to right: $n = 31$, 29, 24, 34, 20, 24, 27, 23, 34, 47 and 43 cells; 3–6 independent experiments each. Two-tailed Student's t-test assuming equal variance was used. ****$P < 0.0001$. **d**, FKBP recruitment rate constants derived from exponential regression of cytosolic FKBP signal decay imaged with confocal microscopy over 10-s intervals. sFRB$_{1C}$ + sFRB$_{1N}$ and FRB groups use identical plasmid constructs as leftmost and rightmost columns, respectively in **b**. Data are presented as mean values ± s.d. From left to right: $n = 9$ and 8 cells, 4–5 independent experiments each. Two-tailed Student's t-test assuming equal variance was used. **$P < 0.0001$. Scale bar, 5 μm.

scans reflect the cytosol to PM localization shift before and 9 min after rapamycin administration (Fig. 2b). Percentage change in mCh–FKBP PM/cytosol ratios derived from line scans was positive for all sFRB pairs tested; values were not significantly different between $sFRB_1$, $sFRB_2$ and $sFRB_3$ and FL FRB ($P = 0.613$, 0.057, 0.579, respectively, Fig. 2c). However, no $sFRB_C$ half could recruit FKBP to the PM without coexpression of its cognate $sFRB_N$ half and vice versa ($P < 0.0001$ for all cases, Fig. 2c). These results suggest that with rapamycin addition, PM-localized sFRB halves are as efficient as full-length FRB in recruiting FKBP, but each sFRB half cannot independently recruit FKBP. However, without FKBP overexpression, sFRB halves can still dimerize (Supplementary Fig. 3), as shown by rapamycin-dependent recruitment of cytosolic $sFRB\chi_C$ to PM-localized Lyn–YFP–$sFRB\chi_N$ ($\chi = 1, 2, 3$) (YFP, yellow fluorescent protein). This is most likely due to endogenous FKBP–rapamycin complexes in the cell[21], and/or due to rapamycin alone bringing sFRB pairs together. sFKBP pairs were also screened, and three out of four split sites ($\chi = 1, 2, 3$) could recruit FRB (Fig. 3f and Supplementary Fig. 4).

Kinetics of cytosolic FKBP translocation to the PM was determined from exponential regression of cytosolic FKBP intensity decay. The rate constant of cytosolic FKBP signal decay with FL FRB was significantly higher than with the $sFRB_1$ pair ($0.085 \pm 0.0075\ s^{-1}$ versus $0.058 \pm 0.0047\ s^{-1}$, $P = 0.008$; Fig. 2d), indicating that $sFRB_1$ has slower FKBP recruitment kinetics after rapamycin addition. The timescale of FKBP recruitment by the $sFRB_1$ pair, however, still falls within the minutes range. To test for irreversibility, cells expressing PM-localized Lyn–YFP–$sFRB\chi_N$, cytosolic CFP–$sFRB\chi_C$ ($\chi = 1$, 2, 3) and cytosolic mCh–FKBP were incubated with rapamycin for 30 min. Samples were then washed ten times, and cells showing trimerization were imaged over 30 min (Supplementary Fig. 5a). No appreciable decrease in PM-to-cytosol ratio was detected for either CFP–sFRBχ or mCh–FKBP (Supplementary Fig. 5b), indicating that sFRB CIT systems are practically irreversible, similar to CID. To test for orthogonality, we assessed $sFRB_N$ with $sFRB_C$ halves split at different sites for rapamycin-based FKBP binding. sFRB pairs are nonorthogonal, but three additional sFRB pairs ($sFRB_{1N}$–$sFRB_{3C}$, $sFRB_{2N}$–$sFRB_{1C}$, $sFRB_{2N}$–$sFRB_{3C}$) were identified to trimerize with FKBP (Supplementary Fig. 6).

Structural validation of split FKBP. First, we solved the crystal structure of the FKBP12–rapamycin–FRB (T2098L) complex to examine whether the T2098L affects the overall conformation and/or the interaction with rapamycin. The crystal structure of FKBP12–rapamycin–FRB (T2098L) determined at a 2.20-Å resolution (Fig. 3a) shows only 0.61 Å of the average root-mean-square deviation (r.m.s.d.) for Cα atoms to the wildtype (WT) FRB-containing complex (PDB ID 1FAP), indicating that the both structures are in almost perfect agreement. Also, the major interactions between FRB (T2098L), FKBP12 and rapamycin were the same as in the WT FRB–FKBP12–rapamycin complex (Fig. 3b). Hence, we confirmed that the T2098L mutation of FRB does not affect the overall conformation and the interactions with rapamycin.

Next, we attempted to purify sFRBχ and sFKBPχ fragments and reconstitute their complexes to structurally validate our split strategy. We could purify $sFKBP_{1N}$ as a maltose binding protein (MBP) fusion protein by an *Escherichia coli* expression system although we could not obtain the $sFRB\chi_N$ fragments as a soluble protein. Therefore, we aimed to structurally validate whether $sFKBP_{1N}$ and $sFKBP_{1C}$ form a functional $sFKBP_1$ complex. First, we observed that $sFKBP_{1N}$ and $sFKBP_{1C}$ can form a stoichiometric $sFKBP_1$ complex at 10 μM, dependent on the addition of rapamycin (Supplementary Fig. 7). We then solved crystal structures of $sFKBP_1$–rapamycin and $sFKBP_1$–rapamycin–FRB (T2098L) complexes at 2.92–3.11-Å resolution (Fig. 3c,d). In both structures, $sFKBP_{1N}$ and $sFKBP_{1C}$ formed the same secondary structure as FKBP12, showing only 0.38 and 0.42 Å of the average r.m.s.d. for Cα atoms to the corresponding region of the intact FKBP12 protein, respectively. The interactions between $sFKBP_1$ and rapamycin are completely conserved in both structures. Finally, the overall structure of $sFKBP_1$–rapamycin–FRB (T2098L) shows only 0.79 Å of the average r.m.s.d. to the intact FKBP12–rapamycin–FRB (T2098L) complex, without disrupting hydrogen bonds and main hydrophobic interactions to FRB and rapamycin (Fig. 3e). These results indicate that, in vitro, split FKBP fragments form a functional FKBP protein that is structurally indistinguishable from intact FKBP protein.

CIT at organelle membrane junction sites. Membrane contact sites (MCS) or junctions are regions of close inter-organellar membrane apposition where unique signaling can occur[4,22,23]. MCS are widespread among almost all membrane-bound organelles[24,25], and local MCS molecular tethers and actuators[26] regulate processes ranging from calcium[27–29] and lipid transport[30] to organelle fission[31,32]. Most MCS regulate multiple functions, and local MCS proteins play compensatory roles, such that few MCS have been completely ablated by the knockdown or knockout of a single gene[33]. These confounding conditions make rapidly inducible perturbation attractive for studying MCS, as supported by previous studies[4,22,23,34]. As proof-of-principle, we used CIT to target cytosolic protein to ER–mitochondria and ER–PM MCS, demonstrating its potential as a generalizable recruitment-based screen for MCS function (Fig. 4a).

To recruit cytosolic protein to ER–PM junctions, we coexpressed PM-targeted $sFRB_{1N}$ (Lyn–CFP–$sFRB_{1N}$) and ER-targeted $sFRB_{1C}$ (YFP–$sFRB_{1C}$–Cb5) with cytosolic mCh–FKBP (Fig. 4a). After rapamycin addition, ER and PM tethering formed patches that colocalize with mCh–FKBP (Fig. 4b and Supplementary Video 1). Pairwise image correlation between all three image wavelengths all significantly increased after rapamycin ($P < 0.0001$, Fig. 4d), suggesting that the CIT system can recruit cytosolic protein to the ER–PM MCS. When we removed $sFRB_{1N}$ (using Lyn–CFP only) or $sFRB_{1C}$ (using only YFP–Cb5), trimerization could not be observed

Fig. 3 | Crystal structure of the split and unsplit FKBP–rapamycin–FRB (T2098L) complexes. a, Superimposition of FKBP12–rapamycin–FRB (T2098L) complex crystal structure (yellow, green and magenta) with that of FKBP12–rapamycin–FRB (WT; PDB ID 1FAP, gray). T2098L is shown in orange. **b**, Magnified view of the rapamycin-interacting region of FKBP12–rapamycin–FRB complexes (color-coded as in **a**). Hydrogen bonds are shown as dashes. **c**, Ribbon (left) and topology (right) diagrams of the $sFKBP_{1N}$ (cyan), $FKBP_{1C}$ (yellow) and rapamycin (green) complex. **d**, Crystal structure of sFKBP1–rapamycin–FRB (T2098L). Left, sFKBP1 (cyan and yellow), rapamycin (green) and FRB (T2098L, magenta) is depicted as a ribbon diagram. Right, electron density of rapamycin. Rapamycin is depicted as a stick model with a 2Fo–Fc electron density (blue mesh) contoured at 1.5 σ. Residues of $sFKBP_{1C}$ (yellow) and FRB (T2098L) (magenta) involved in the interaction with rapamycin are labeled and shown as a line model. **e**, LigPlot diagrams showing critical contacts around rapamycin. Left, FKBP12–rapamycin–FRB (T2098L). Right, $sFKBP_1$–rapamycin–FRB (T2098L). Rapamycin (green) and key residues of unsplit (left) and split (right) FKBP proteins (yellow, Y27 of $sFKBP_{1N}$ in cyan) and those of FRB (magenta, T2098L in orange) are depicted in a ball and stick model. Carbon, nitrogen and oxygen are gray, blue and red balls, respectively. Hydrogen bond and hydrophobic interaction are shown as a black dashed line and a red arc of a circle, respectively. **f**, Percentage change in FRB–mCh PM-to-cytosolic ratio before and after rapamycin addition. Each sFKBP pair (N + C) is compared with N- or C-terminal halves only (N or C), full-length FKBP or no FKBP in FRB recruitment. Data are presented as mean values ± s.d. From left to right: $n = 21$, 28, 38, 20, 39, 38, 25, 25, 21, 28, 32, 33, 29 and 31 cells; 3–13 independent experiments each. Two-tailed Student's *t*-test assuming equal variance used. ****$P < 0.0001$; NS, not significant.

(Extended Data Fig. 1a,b, left and center) with no increase in image correlation coefficients between all three signals. However, when mCh alone was expressed instead of mCh–FKBP, ER–PM tethering still occurred, albeit with no mCh recruitment to the site, and the image correlation coefficient between the ER and PM signals significantly increased (Extended Data Fig. 1a,b, right).

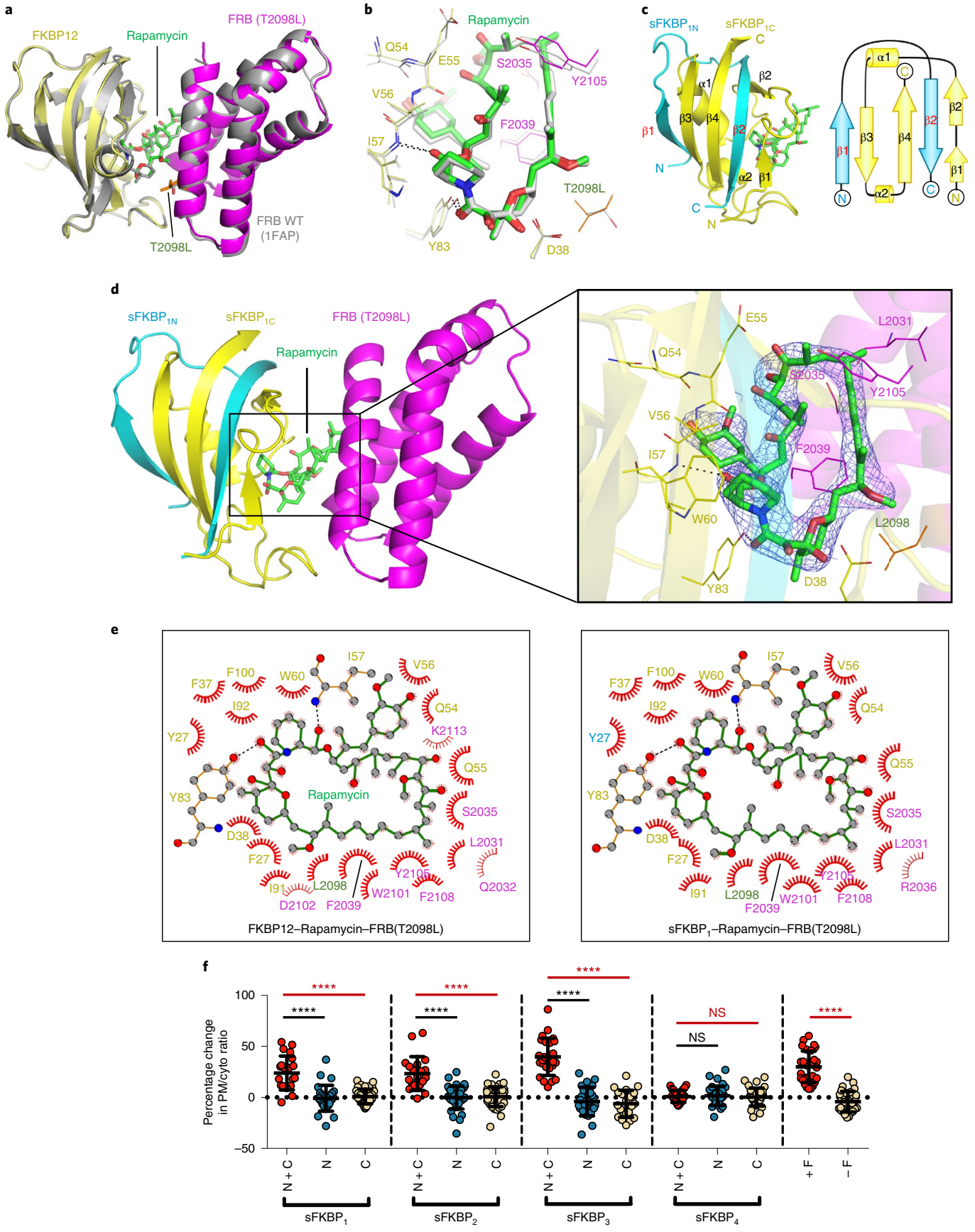

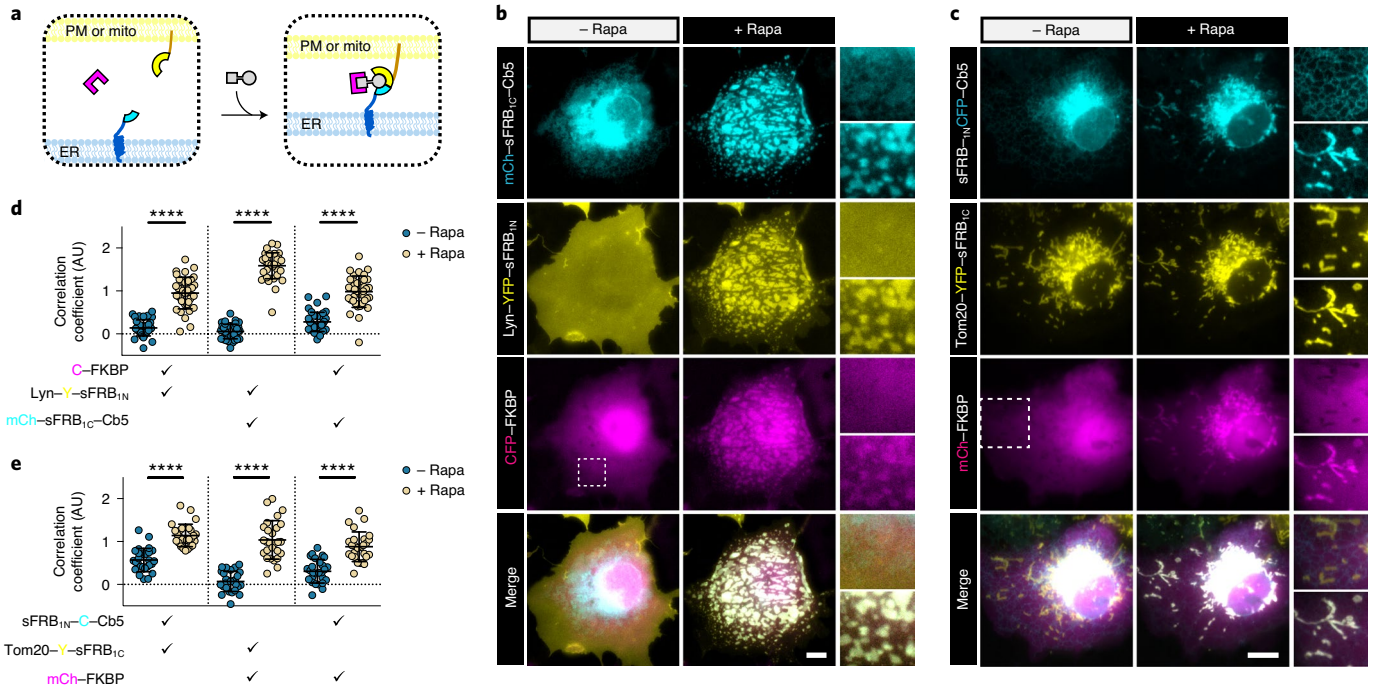

Fig. 4 | CIT-based recruitment of cytosolic protein to ER–PM and ER–mitochondria MCS. a, Targeting cytosolic FKBP (magenta) to ER–PM or ER–mitochondria MCS. sFRB halves (cyan and yellow) targeted to two organelles recruit FKBP in a rapamycin-dependent manner. **b**, Cos-7 cells expressing mCh–sFRB$_{1C}$-Cb5, Lyn-Y-sFRB$_{1N}$ and CF before and 12 min after rapamycin for CF recruitment at ER–PM MCS. **c**, Cos-7 cells expressing sFRB$_{1N}$–C–Cb5, Tom20-Y-sFRB$_{1C}$, and CF before and 12 min after rapamycin for CF recruitment at ER–mitochondria MCS. **d**,**e**, Trimerization quantification between the three signals before and after rapamycin. Check marks specify each combination of two wavelengths used in calculating pairwise Fisher's transformation of Pearson's correlation coefficients. Data are presented as mean values ± s.d. Two-tailed Student's *t*-test assuming equal variance was used to compare correlations before and after 100 nM rapamycin. ****$P < 0.0001$. **d**, $n = 38$ cells, three independent experiments. **e**, $n = 27$ cells, three independent experiments. Scale bars, 10 μm.

We also used sFKBP to recruit cytosolic FRB–mCh to ER–PM junctions. Cells showed undetectable or prominent FRB–mCh recruitment at ER–PM junctions before and 1 h after rapamycin addition (Extended Data Fig. 2a,b, respectively). Imaging showed slower cytosolic protein recruitment compared to sFRB trimerization (12 min versus 1 h, Supplementary Video 1 versus Supplementary Video 2). Pairwise image correlation significantly increased between ER and PM channels ($P < 0.0001$), cytosolic FRB–mCh and ER channels ($P = 0.030$), and not significantly between cytosolic FRB–mCh and PM channels ($P = 0.16$) (Extended Data Fig. 2c). Because sFKBP was less efficient compared to sFRB in targeting cytosolic proteins to ER–PM junctions, we decided to continue with only sFRB for MCS applications.

We also applied sFRB CIT to ER–mitochondria junctions. Complimentary sFRB pairs were expressed on the ER (sFRB$_{1N}$–CFP–Cb5) and mitochondria (Tom20–YFP–sFRB$_{1C}$), and after rapamycin addition translocated mCh–FKBP to ER–mitochondria MCS (Fig. 4c and Supplementary Video 3). Pairwise image correlation coefficients increased for all three wavelengths, indicating successful trimerization ($P < 0.0001$ all cases, Fig. 4e). Likewise, removal of sFRB$_{1N}$ (Lyn–YFP) and sFRB$_{1C}$ (mCh–Cb5) yielded no translocation of mCh–FKBP to ER–mitochondria MCS after rapamycin addition (Extended Data Fig. 3a,b, left and center), whereas removal of FKBP resulted in increased colocalization between the ER and mitochondria components, without colocalization of mCh (Extended Data Fig. 3a,b, right).

CIT induces tri-organellar MCS. Multi-spectral imaging has revealed that ER–mitochondria MCS makes frequent contact with Golgi, peroxisomes and lipid droplets, hinting at tri-organellar MCS[25]. ER–mitochondria MCS also marks regions of autophagosome formation[35]. We therefore speculated that a tri-organelle ER–PM–mitochondria junction site could exist due to the existence of ER–PM, ER–mitochondria and PM–mitochondria MCS, and their shared function in Ca^{2+} signaling. Using CIT to determine whether a tri-organellar junction could be synthetically formed between the PM, ER and mitochondria, we coexpressed sFRB$_{1C}$ localized to the PM (Lyn–CFP–sFRB$_{1C}$), sFRB$_{1N}$ to the ER (YFP–sFRB$_{1N}$–Cb5) and FKBP to the mitochondria (Tom20–mCh–FKBP) in Cos-7 cells (Fig. 5a–c). Fifteen minutes after rapamycin addition, PM, ER and mitochondrial signals colocalized (Fig. 5b,c and Supplementary Video 4); all correlation coefficients increased ($P < 0.0001$; Fig. 5d). When sFRB$_{1C}$, sFRB$_{1N}$ or FKBP were each removed, trimerization no longer occurred after rapamycin addition (Extended Data Fig. 4a,b, left and right), but removal of FKBP still resulted in colocalization of ER–PM signals (Extended Data Fig. 4a,b, center). These results show that CIT can induce PM–ER–mitochondria tethering, and serves as a detection method for potential tri-organellar MCS formation between three organelles.

Localized PI(4,5)P$_2$ depletion at ER–PM junctions. Functions of ER–PM MCS include Ca^{2+} re-entry and lipid homeostasis, with focus shifting to the latter in recent years[36]. One major topic in the field is the regulation of secondary lipid messenger PI(4,5)P$_2$ (PIP$_2$) and its precursor PI(4)P. PM resident PIP$_2$ and its precursor PI(4)P levels are often in flux during signal transduction. ER–PM junctions serve as a bridge connecting the PM and ER, where local proteins regulate PM lipid homeostasis by using the ER as a reservoir or a sink, depending on the needs of the PM[23,34,37]. While methods exist to perturb PM lipid composition or locally deplete PIP$_2$ from the

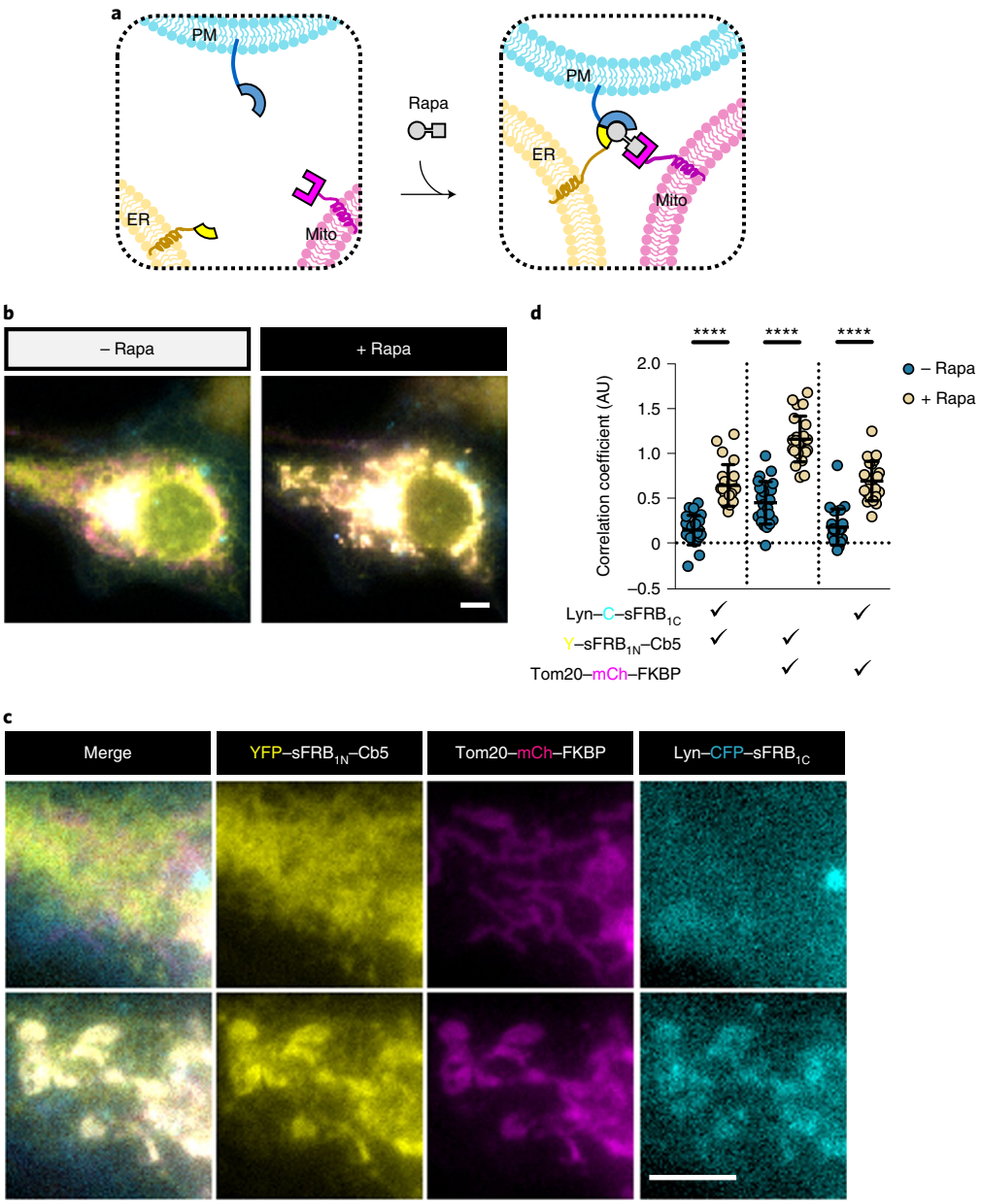

Fig. 5 | Tri-organellar junction formation by CIT. a, Trimerization of CIT components targeted to ER, mitochondria and PM by rapamycin. **b**, Cos-7 cell expressing Y-sFRB$_{1N}$-Cb5, Tom20-mCh-FKBP and Lyn-C-sFRB$_{1C}$ before and 15 min after rapamycin addition. **c**, Higher magnification of the cell shown in **b**, including individual fluorescence channels. **d**, Quantification of trimerization extent through pairwise correlation of Fisher's transformation of Pearson's correlation coefficient between three wavelengths. Data are presented as mean values ± s.d. Two-tailed Student's *t*-test assuming equal variance was used to compare correlations before and after 100 nM rapamycin. ****$P < 0.0001$. $n = 23$ cells; four independent experiments. Scale bars, 5 µm.

PM[38], the means of perturbing lipids only at ER–PM junctions have yet to be established.

To achieve local PIP$_2$ depletion, we coexpressed PM-localized sFRB$_{1N}$ (Lyn–Clover–FRB$_{1N}$), ER-localized sFRB$_{1C}$ (iRFP–FRB$_{1C}$–Cb5), cytosolic CFP–FKBP (CF) fused to 5-phosphatase INP54P (331) (CF–INP54P) and PIP$_2$ biosensor mRuby–PH–PLCδ in Cos-7 cells (Fig. 6a). After rapamycin addition, CF–INP54P was recruited to ER–PM junctions, with a marked pattern of reduction in mRuby–PH–PLCδ intensity (Fig. 6b, left, and Supplementary Video 5). In contrast, recruitment of INP54P phosphatase-dead mutant CF–INP54P D281A or CF alone did not reduce mRuby–PH–PLCδ intensity (Fig. 6b, center and left and Supplementary Videos 6 and 7, respectively). Line-scan analysis (Fig. 6c) further confirmed the PIP$_2$ depletion confined to the ER–PM junctions (gray shades). PIP$_2$ levels in the regions outside ER–PM contact sites remained intact, accordingly forming a sharp gradient of PIP$_2$ immediately outside the junctions. Junctional PIP$_2$ reduction occurred in areas of high (teal dashed squares, Fig. 6b) compared to low ER–PM junction formation (orange dashed squares) 5 min after CF–INP54P recruitment by rapamycin, reflected in percentage change in mRuby–PH–PLCδ intensity in the respective regions ($P < 0.0001$, Fig. 6d). CF–INP54P D281A recruitment to ER–PM rich regions only slightly decreased mRuby–PH–PLCδ intensity relative to outside these regions ($P = 0.0358$, Fig. 6d). CF recruitment to ER–PM rich regions did not significantly change mRuby–PH–PLCδ intensity compared to outside these regions ($P = 0.5189$, Fig. 6d). The same analysis conducted over time indicates that junctional PIP$_2$ reduction took place as early as 2 min after INP54P recruitment with

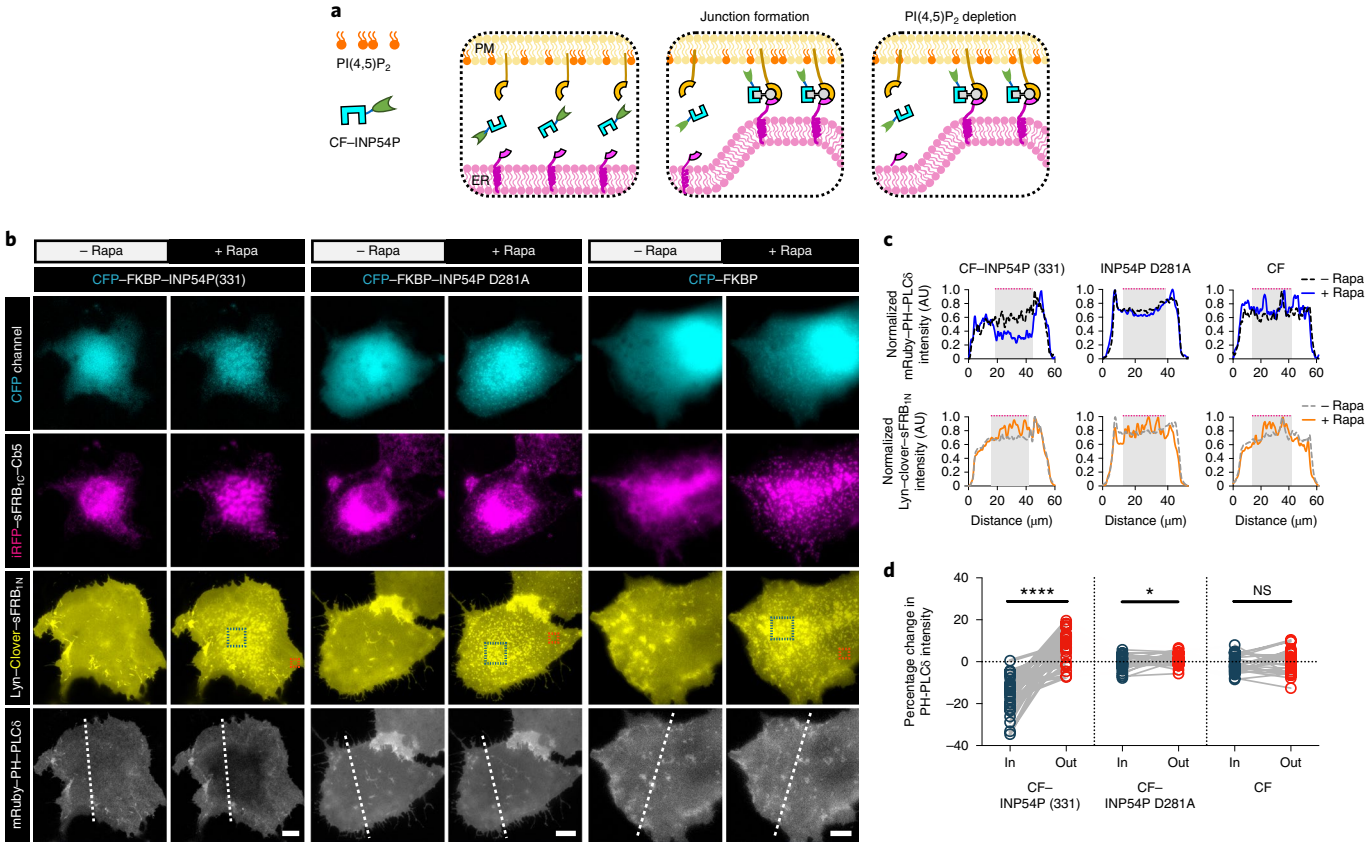

Fig. 6 | CIT induces local PI(4,5)P_2 depletion at ER–PM MCS. a, Schematic of CIT-induced PI(4,5)$_2$ depletion. CF–INP54P is recruited to ER–PM MCS by ER and PM-localized sFRB halves. On junction formation (middle panel), INP54P accesses PM PI(4,5)P_2 leading to local PI(4,5)P_2 depletion (right panel). **b**, Comparing effects of ER–PM MCS recruitment of functional CF–INP54P (331) against phosphatase-dead mutant CF–INP54P (D281A) and CF alone. Cos-7 cells also express Lyn–Clover–sFRB$_{1N}$, iRFP–sFRB$_{1C}$–Cb5 and mRuby–PH–PLCδ, a PI(4,5)P_2 biosensor. Timelapse epifluorescence microscopy taken before and 5 min after rapamycin addition. Teal and orange dotted boxes indicate regions inside and outside ER–PM MCS, respectively. **c**, Normalized intensity of mRuby–PH–PLCδ PI(4,5)P_2 biosensor line scans from **b**. Gray shaded regions with dotted magenta lines indicate high ER–PM junction formation. **d**, Intensities of mRuby–PH–PLCδ PI(4,5)P_2 biosensor of user-defined ROI inside and outside ER–PM MCS. Analyzed with two-tailed paired Students *t*-test assuming equal variance. $^*P < 0.05$; $^{****}P < 0.0001$; NS, not significant. Pairs from left to right: $n = 28$, 25 and 28 cells; four independent experiments each. Scale bar, 10 μm.

rapamycin (Extended Data Fig. 5), and with continued decrease in PIP_2 levels even after 10 min. Lack of PIP_2 reduction in CF–INP54P D281A and CF controls further suggests that molecular crowding effects of CIT has minimal impact on the ability of mRuby–PH–PLCδ to detect PIP_2. These results collectively demonstrate that CIT-based recruitment of INP54P can locally deplete PIP_2 at ER–PM junctions.

Discussion

In this study, we designed, developed and implemented a CIT system by rationally splitting proteins of the FKBP or FRB–CID system. The CIT tool is small, robust and trimerizes on a timescale of seconds to minutes. CIT responds to one chemical stimulus, and has clear trimeric stoichiometry according to crystallography results. We used CIT to rapidly target cytosolic protein exclusively to ER–PM and ER–mitochondria MCS, induce tri-organellar ER–mitochondria-PM junctions and locally deplete PIP_2 at ER–PM MCS. We believe that our ability to achieve CIT is attributed to the unique cooperativity of the FKBP–FRB–CID. This efficient CIT system would be otherwise highly difficult to achieve de novo, as engineering sequential cooperativity at protein interfaces would be necessary.

As FKBP binding affinity for rapamycin is over 10,000-fold higher than FRB (0.2 versus 26 μM)[13], we believe that sFRB CIT is first achieved by formation of FKBP–rapamycin complexes, followed by sFRB halves binding. For the sFKBP system, our crystallization data show that rapamycin can dimerize sFKBP$_1$ halves in the absence of FRB. Gel filtration analysis indicates sFKBP$_1$ dimerizes saturatively at a protein concentration of 10 μM in the presence of rapamycin (Supplementary Fig. 7), suggesting that the dissociation constant, switchable by rapamycin, between FKBP$_{1N}$ and sFKBP$_{1C}$ is less than a single digit micromolar concentration. We believe that in the sFKBP system, rapamycin brings together sFKBP with micromolar affinity and then sFKBP–rapamycin complex recruits full-length FRB. Our results suggest that the prevalent mechanism of trimerization for both sFRB and sFKBP CIT systems involves an initial complex formation of FKBP–rapamycin or sFKBP–rapamycin complexes, followed by the binding of sFRB or FRB, respectively.

Components of sFRB and sFKBP CIT systems are small; sFRB$_{1N}$ and sFRB$_{1C}$ are 5 and 6.3 kDa, respectively. While sFRB$_{\chi N}$ and sFRB$_{\chi C}$ halves do not function orthogonally, we discovered three additional sFRB pairs (sFRB$_{1N}$–sFRB$_{3C}$, sFRB$_{2N}$–sFRB$_{1C}$, sFRB$_{2N}$–sFRB$_{3C}$) that trimerize with FKBP. In total, we generated six sFRB pairs capable of trimerization, increasing the likelihood of successful CIT implementation across biological systems. Further, the high degree of similarity between WT FRB and FRB T2098L in our crystallization data suggests that that WT or other FRB variants may be split similarly to generate additional CIT systems that respond to various rapamycin analogs.

Depletion of PIP_2 at ER–PM junctions (Fig. 6) catalyzes further investigation of local PIP_2 depletion at the ER–PM junction compared to global PIP_2 depletion at the PM; it may provide insight into the relationship between lipid transfer and Ca^{2+} entry at the ER–PM junction, as they share common players such as PIP_2 and PI(4)P. Additionally, the tri-organellar PM–ER–mitochondria junction formed through CIT indirectly suggests that these three organelles have the potential of interacting. In the future, CIT can be a powerful tool to validate and perturb other tri-organellar MCS, such as the ER–mitochondria–Golgi junction[25].

In all, we developed a trimerization tool capable of cell signaling manipulation in new ways. MCS targeting in this study demonstrated the enhanced spatiotemporal specificity CIT has over CID. We see potential for the tool beyond its role in future screens for studying MCS. Hundreds of available and validated CID-based actuators can now be readily retrofitted with CIT components to modulate various cell signaling pathways[1,2,6], including kinase modulation[39], and produce increasingly sophisticated, tunable switches and logic gates. Trimerization is also a common mechanism in nature, and CIT-based mimicry may deduce the significance of trimerization in these systems. By introducing a third component to be recruited to two others with one chemical stimulus, CIT introduces a new tool to chemical, synthetic and cell biology toolkits.

Online content

Any methods, additional references, Nature Research reporting summaries, source data, extended data, supplementary information, acknowledgements, peer review information; details of author contributions and competing interests; and statements of data and code availability are available at https://doi.org/10.1038/s41592-020-0913-x.

Received: 16 March 2020; Accepted: 6 July 2020;
Published online: 3 August 2020

References

1. Fegan, A., White, B., Carlson, J. C. & Wagner, C. R. Chemically controlled protein assembly: techniques and applications. *Chem. Rev.* **110**, 3315–3336 (2010).
2. DeRose, R., Miyamoto, T. & Inoue, T. Manipulating signaling at will: chemically-inducible dimerization (CID) techniques resolve problems in cell biology. *Pflug. Arch.* **465**, 409–417 (2013).
3. Spencer, D. M., Wandless, T. J., Schreiber, S. L. & Crabtree, G. R. Controlling signal transduction with synthetic ligands. *Science* **262**, 1019–1024 (1993).
4. Komatsu, T. et al. Organelle-specific, rapid induction of molecular activities and membrane tethering. *Nat. Methods* **7**, 206–208 (2010).
5. Haruki, H., Nishikawa, J. & Laemmli, U. K. The anchor-away technique: rapid, conditional establishment of yeast mutant phenotypes. *Mol. Cell* **31**, 925–932 (2008).
6. Putyrski, M. & Schultz, C. Protein translocation as a tool: the current rapamycin story. *FEBS Lett.* **586**, 2097–2105 (2012).
7. Miyamoto, T. et al. Rapid and orthogonal logic gating with a gibberellin-induced dimerization system. *Nat. Chem. Biol.* **8**, 465–470 (2012).
8. Stanton, B. Z., Chory, E. J. & Crabtree, G. R. Chemically induced proximity in biology and medicine. *Science* **359**, eaao5902 (2018).
9. Ma, D., Peng, S. & Xie, Z. Integration and exchange of split dCas9 domains for transcriptional controls in mammalian cells. *Nat. Commun.* **7**, 13056 (2016).
10. Lambright, D. G. et al. The 2.0 A crystal structure of a heterotrimeric G protein. *Nature* **379**, 311–319 (1996).
11. Higashi, T. & Miller, A. L. Tricellular junctions: how to build junctions at the TRICkiest points of epithelial cells. *Mol. Biol. Cell* **28**, 2023–2034 (2017).
12. Hennecke, J. & Wiley, D. C. T cell receptor-MHC interactions up close. *Cell* **104**, 1–4 (2001).
13. Banaszynski, L. A., Liu, C. W. & Wandless, T. J. Characterization of the FKBP·rapamycin·FRB ternary complex. *J. Am. Chem. Soc.* **127**, 4715–4721 (2005).
14. Choi, J., Chen, J., Schreiber, S. L. & Clardy, J. Structure of the FKBP12–rapamycin complex interacting with the binding domain of human FRAP. *Science* **273**, 239–242 (1996).
15. Stankunas, K. et al. Rescue of degradation-prone mutants of the FK506–rapamycin binding (FRB) protein with chemical ligands. *Chem. Bio. Chem.* **8**, 1162–1169 (2007).
16. Liberles, S. D., Diver, S. T., Austin, D. J. & Schreiber, S. L. Inducible gene expression and protein translocation using nontoxic ligands identified by a mammalian three-hybrid screen. *Proc. Natl Acad. Sci. USA* **94**, 7825–7830 (1997).
17. Bayle, J. H. et al. Rapamycin analogs with differential binding specificity permit orthogonal control of protein activity. *Chem. Biol.* **13**, 99–107 (2006).
18. Dagliyan, O. et al. Computational design of chemogenetic and optogenetic split proteins. *Nat. Commun.* **9**, 4042 (2018).
19. Dagliyan, O. et al. Engineering extrinsic disorder to control protein activity in living cells. *Science* **354**, 1441–1444 (2016).
20. Dagliyan, O., Dokholyan, N. V. & Hahn, K. M. Engineering proteins for allosteric control by light or ligands. *Nat. Protoc.* **14**, 1863–1883 (2019).
21. Belshaw, P. J., Schoepfer, J. G., Liu, K. Q., Morrison, K. L. & Schreiber, S. L. Rational design of orthogonal receptor–ligand combinations. *Angew. Chem. Int. Ed. Engl.* **34**, 2129–2132 (1995).
22. Varnai, P., Toth, B., Toth, D. J., Hunyady, L. & Balla, T. Visualization and manipulation of plasma membrane-endoplasmic reticulum contact sites indicates the presence of additional molecular components within the STIM1-Orai1 Complex. *J. Biol. Chem.* **282**, 29678–29690 (2007).
23. Dickson, E. J. et al. Dynamic formation of ER-PM junctions presents a lipid phosphatase to regulate phosphoinositides. *J. Cell Biol.* **213**, 33–48 (2016).
24. Phillips, M. J. & Voeltz, G. K. Structure and function of ER membrane contact sites with other organelles. *Nat. Rev. Mol. Cell Biol.* **17**, 69–82 (2016).
25. Valm, A. M. et al. Applying systems-level spectral imaging and analysis to reveal the organelle interactome. *Nature* **546**, 162–167 (2017).
26. Prinz, W. A. Bridging the gap: membrane contact sites in signaling, metabolism, and organelle dynamics. *J. Cell Biol.* **205**, 759–769 (2014).
27. Luik, R. M., Wang, B., Prakriya, M., Wu, M. M. & Lewis, R. S. Oligomerization of STIM1 couples ER calcium depletion to CRAC channel activation. *Nature* **454**, 538–542 (2008).
28. Liou, J. et al. STIM is a Ca^{2+} sensor essential for Ca^{2+}-store-depletion-triggered Ca^{2+} influx. *Curr. Biol.* **15**, 1235–1241 (2005).
29. Rizzuto, R. et al. Close contacts with the endoplasmic reticulum as determinants of mitochondrial Ca^{2+} responses. *Science* **280**, 1763–1766 (1998).
30. Levine, T. & Loewen, C. Inter-organelle membrane contact sites: through a glass, darkly. *Curr. Opin. Cell Biol.* **18**, 371–378 (2006).
31. Friedman, J. R. et al. ER tubules mark sites of mitochondrial division. *Science* **334**, 358–362 (2011).
32. Rowland, A. A., Chitwood, P. J., Phillips, M. J. & Voeltz, G. K. ER contact sites define the position and timing of endosome fission. *Cell* **159**, 1027–1041 (2014).
33. Helle, S. C. et al. Organization and function of membrane contact sites. *Biochim. Biophys. Acta* **1833**, 2526–2541 (2013).
34. Zewe, J. P., Wills, R. C., Sangappa, S., Goulden, B. D. & Hammond, G. R. SAC1 degrades its lipid substrate PtdIns4P in the endoplasmic reticulum to maintain a steep chemical gradient with donor membranes. *eLife* **7**, e35588 (2018).
35. Hamasaki, M. et al. Autophagosomes form at ER–mitochondria contact sites. *Nature* **495**, 389–393 (2013).
36. Saheki, Y. & De Camilli, P. Endoplasmic reticulum-plasma membrane contact sites. *Annu. Rev. Biochem.* **86**, 659–684 (2017).
37. Chang, C. L. & Liou, J. Phosphatidylinositol 4,5-bisphosphate homeostasis regulated by Nir2 and Nir3 proteins at endoplasmic reticulum-plasma membrane junctions. *J. Biol. Chem.* **290**, 14289–14301 (2015).
38. Idevall-Hagren, O., Dickson, E. J., Hille, B., Toomre, D. K. & De Camilli, P. Optogenetic control of phosphoinositide metabolism. *Proc. Natl Acad. Sci. USA* **109**, E2316–E2323 (2012).
39. Karginov, A. V., Ding, F., Kota, P., Dokholyan, N. V. & Hahn, K. M. Engineered allosteric activation of kinases in living cells. *Nat. Biotechnol.* **28**, 743–747 (2010).

Publisher's note Springer Nature remains neutral with regard to jurisdictional claims in published maps and institutional affiliations.

© The Author(s), under exclusive licence to Springer Nature America, Inc. 2020

Methods

Cell culture and transfection. HeLa and Cos-7 cells were maintained at 37 °C, 5% CO_2 and 95% humidity in Dulbecco's modified Eagle's medium (DMEM) supplemented with 10% FBS and 1% pen/strep (Gibco). The day before imaging, cells were detached with 5% Trypsin-EDTA (Gibco) and gathered for reverse transfection with FuGENE HD (Promega). As a general rule, cotransfection of split and unsplit proteins used a split protein to unsplit protein plasmid ratio of 20:1 for sFRB CIT experiments and a ratio of 10:1 for sFKBP CIT. Before imaging, cell medium in samples was replaced with Dulbecco's phosphate-buffered saline containing Ca^{2+} and Mg^{2+} for imaging <30 min or fresh DMEM growth media for imaging >30 min. Cells were transfected with constructs at adjusted relative plasmid ratios and incubated for 16–24 h before imaging.

DNA plasmid construction. Constructs used to determine working split proteins were based off Clontech C1 and N1 backbones with various fluorophores. A 5xSAGG flexible linker oligo was annealed was inserted between KpnI and SalI restriction sites of both C1 and N1 backbones. Lyn or CAAX oligo DNA fragments were subsequently annealed and ligated into C1 or N1 backbones containing 5xSAGG linkers. Then, FRB or FKBP fragments were cloned and inserted between KpnI and BamHI or HindIII and SalI for C1 and N1 vectors, respectively. To obtain non-Lyn or CAAX versions of the proteins, the portion containing fluorescent protein with split FRB or FKBP fragments were cut and pasted into C1 or N1 backbone vectors lacking Lyn or CAAX. YFP–$sFRB_{1N}$–Cb5 was generated by deletion mutagenesis of previously reported YFP–FRB–Cb5 (ref. [4]). ER-targeting sequence Cb5 was amplified by PCR and subcloned into a $sFRB_{1N}$-C backbone from $sFRB_{1N}$–C–Cb5 to generate $sFRB_{1N}$–C–Cb5. CF–INP54P (331) and CF–INP54P (D281A) were from a previous report[40]. All plasmids were verified by Sanger sequencing.

Live-cell imaging. Most imaging was conducted on a IX71 microscope (Olympus) with a ×63 objective (and ×1.6 zoom) and an ORCA-Flash4.0 LT Digital CMOS camera (Hamamatsu). Rate constant of FKBP recruitment by $sFRB_1$ was imaged at 10-s intervals with a spinning disc confocal, inverted Axiovert 200 (Zeiss) with a ×40 objective and an Orca ER CCD camera (Hamamatsu). Both microscopes were driven by Metamorph 7.5 imaging software (Molecular Devices). Four-color imaging in Fig. 4 was conducted with an Eclipse Ti microscope (Nikon) with a ×60 objective (and ×1.5 zoom) and a Zyla 4.2 sCMOS camera (Andor), driven by NIS Elements software (Nikon). Unless otherwise indicated imaging was done at 1–3-min intervals for 12–30 min, at times with between 3–5 0.5-µm-spaced z positions. Images analyzed and shown are from a single plane, and not maximum intensity projections. Microscopy experiments applying CIT to MCS were conducted at 37 °C, 5% CO_2 and humidity with a stage top incubation system (Tokai Hit).

Analysis of PM-to-cytosol ratio. PM-to-cytosol ratio was determined through line-scan analysis. Lines through cells were drawn to (1) avoid the nucleus and (2) maximize the two membrane signals on both sides of the cell. Two PM (p_1, p_2) locations based on peak intensities (I) along the line scan were determined visually. The cytosol was defined as midpoint location (m) between p_1 and p_2. A moving average of three was used to determine signal intensity at p_1 and p_2, and a moving average of five at the cytosol location. Then PM-to-cytosol ratio was determined for each PM location, and then averaged. Percentage change was determined from PM-to-cytosol ratio values before and after rapamycin treatment:

$$\text{PM to cytosol ratio} = \frac{5}{3}\frac{\sum_{n=p_1-1}^{p_1+1} I(n) + \sum_{n=p_2-1}^{p_2+1} I(n)}{\sum_{n=m-2}^{m+2} I(n)}$$

Analysis of recruitment rate. Averaged intensities from three regions of interest (ROI) from the cytosol were used to generate exponential decay curves. Averaged intensity timepoints with exponential decay trends were selected for line fitting with an exponential regression to determine the exponential recruitment coefficient. R^2 values were all >0.88.

$$I = Ae^{-(\text{rate constant})t}$$

Analysis of trimerization with Fisher's transform of Pearson's correlation coefficient. Three ROI of about 50×50 pixels were manually positioned for each cell to determine Pearson's correlation using FIJI. ROI were chosen include enough background and organelle to mitigate false correlations. Due to organelle movement and deformation, different ROI were selected for the same cell before and after rapamycin addition. Pairwise Pearson's correlation (between ROI1 and ROI2) was determined among three channels using the built-in MATLAB function corr2, and averaged between three ROIs. Fisher's transform was performed to normalize Pearson's correlation coefficient for later statistical analysis. The overall result is referred to as the correlation coefficient.

$$\text{Correlation coefficient} = \tanh^{-1}(\text{corr2}(\text{ROI1}, \text{ROI2}))$$

Statistical analysis and data visualization. Unless otherwise stated, most statistical analysis was done with unpaired, two-tailed Student's t-test assuming equal distributions. A paired, two-tailed Student's t-test was used in Fig. 6c. PRISM 6 software was used for statistical analysis and data visualization.

Split site prediction. Split sites were determined by selecting nonevolutionarily conserved solvent accessible loops. The Stride program[41] was used to calculate the solvent accessible areas. Loops exceeding 30 Å^2 were selected as potential split sites. Sequence conservation as indicated by Kullback–Liebler conservation scores was determined with MISTIC[42] and FKBP domain and FRB domain sequences used were obtained from PFAM server[43]. Loops with Kullback–Leibler conservation scores less than two were selected as potential split sites. The difference between the native energy of the intact protein and the sum of the energies of the split proteins at a given split site—the split energy—was calculated using the MEDUSA scoring function[44]. Energy wells were indicative of split sites in this study, which differs from the previous implementation of SPELL, which targeted regions outside energy wells[18]. The original SPELL study looked for split proteins sites that minimized the destabilization as these proteins were then fused to a known destabilizer domain (iFKBP)[18]. This approach ensures the prevention of the split part association in the absence of rapamycin.

Crystallography. *Protein expression and purification.* For structural analysis, complementary DNA encoding the $sFKBP_{1N}$ (residues 1–32 of human FKBP12) was amplified by PCR and subcloned into a pET28a(+) derivative vector, which has a MBP-encoding sequence inserted after an N-terminal polyhistidine tag. The construct contained a tobacco etch virus (TEV) protease recognition site at the junction between polyhistidine tag and the MBP sequences. Recombinant $sFKBP_{1N}$ protein was expressed in *E. coli* BL21 (DE3) cells in LB broth at 37 °C until the optical density (OD_{600}) reached 0.8, at which point the temperature was shifted to 18 °C. Protein expression was induced by addition of isopropyl-β-D-thiogalactopyranoside to a final concentration of 250 µM. The cultures were grown for an additional 20 h and harvested by centrifugation. Cell pellets were resuspended in 50 mM of Tris-HCl buffer (pH 7.0) containing 500 mM of NaCl, 20 mM of imidazole and 10% glycerol. Cells were lysed by sonication and clarified by centrifugation. The cell lysate was loaded onto a HisTrap HP column (GE Healthcare), and eluted with 50 mM of Tris-HCl buffer (pH 7.0) containing 500 mM of NaCl, 500 mM of imidazole and 10% glycerol. The N-terminal histidine tag was cleaved by incubating with TEV protease overnight at 4 °C. The protein was further purified using a HiLoad Superdex 200 16/60 size-exclusion column (GE Healthcare) equilibrated with 20 mM of Tris-HCl buffer (pH 8.0) containing 150 mM NaCl and 5 mM DTT. The $sFKBP_{1C}$ (residues 33–108 of human FKBP12) was expressed and purified essentially as the same as $sFKBP_{1N}$, except an N-terminal His-SUMO tag was fused instead of the polyhistidine and MBP. The His-SUMO tag was cleaved by SUMO protease overnight at 4 °C. The purified $sFKBP_{1N}$ and $sFKBP_{1C}$ proteins were mixed in a 1:2 molar ratio, and then the mixture was added to a 1 µM of rapamycin solution in 20 mM of Tris-HCl buffer (pH 8.0) containing 150 mM of NaCl, 5 mM of DTT and 10% of DMSO. The $sFKBP_{1N}$, $sFKBP_{1c}$ and rapamycin mixture was filtered and loaded onto a Superdex 200 Increase 10/300 GL column (GE Healthcare) equilibrated with 20 mM Tris-HCl buffer (pH 8.0) containing 150 mM of NaCl and 5 mM of DTT. The eluted peak fractions of the $sFKBP_1$–rapamycin complex were pooled and concentrated to 40 mg ml^{-1}. For binding analysis, 100 µM of MBP–$sFKBP_{1N}$ and 10 µM of SUMO–$sFKBP_{1c}$ were mixed in 20 mM of Tris-HCl buffer (pH 8.0) containing 150 mM of NaCl, 5 mM of DTT and 10% DMSO in the presence or absence of 10 µM of rapamycin. The samples were loaded on the Superdex 200 Increase 10/300 GL column, and fractions eluted around 13.8 and 15.4 ml were analyzed by SDS–PAGE. The cDNAs encoding human FKBP12 (residues 1–108) and FKBP12–rapamycin-binding (FRB) domain encompassing residues 2021–2113 of human mTOR (T2098L) were subcloned into pET28a(+) containing an N-terminal polyhistidine-GST tag. The FKBP12 and FRB mutant proteins were expressed and purified essentially the same as $sFKBP_{1N}$. The His-GST tag was cleaved by TEV protease overnight at 4 °C.

Crystallization, data collection and structure determination. Crystallization was performed by the sitting-drop vapor-diffusion method at 20 °C. Crystals of $sFKBP_1$–rapamycin appeared by mixing equal volumes of a 40 mg ml^{-1} of $sFKBP_1$–rapamycin complex solution and a reservoir solution of 100 mM of Na-HEPES buffer (pH 7.5) containing 20% (w/v) PEG 8000. FKBP12–rapamycin–FRB (T2098L) complex was prepared by mixing them at an equimolar ratio and incubating for 60 min on ice. Crystals of FKBP12–rapamycin–FRB (T2098L) appeared at 100 mM of cacodylic acid buffer (pH 6.5) containing 350 mM of zinc acetate and 8% (w/v) isopropanol. $sFKBP_1$–rapamycin–FRB (T2098L) complex was prepared in the same manner as FKBP12–rapamycin–FRB (T2098L). Crystals of $sFKBP_1$–rapamycin–FRB (T2098L) appeared at 100 mM of Tris-HCl buffer (pH 7.0) containing 200 mM of calcium acetate and 20% (w/v) PEG 3000. All crystals were briefly soaked in a cryoprotectant drop composed of the reservoir solution supplemented with 20% glycerol and then flash-cooled in liquid nitrogen for X-ray diffraction data collection. The datasets were collected at 1.000 Å, 100 K on the beamline BL26B2 at SPring-8) or the beamline X06DA

at the Swiss Light Source. They were processed using the XDS[45] and scaled using AIMLESS supported by other programs of the CCP4 suite[46]. Crystal structures were determined by molecular replacement using MOLREP[47] with the FKBP12–rapamycin–FRB structure (PDB ID 1FAP) and the MBP structure (PDB ID 1ANF) as the search models. Model building was accomplished with Coot[48], and structural refinement was performed with REFMAC[49] and PHENIX[50]. The Ramachandran statistics are as follows: 96.0% favored, 4.0% allowed for $sFKBP_1$–rapamycin; 97.2% favored, 2.8% allowed for FKBP12–rapamycin–FRB (T2098L) and 96.8% favored, 3.2% allowed for $sFKBP_1$–rapamycin–FRB (T2098L). The data collection and refinement statistics are summarized in Supplementary Table 1. The structural models in the figures were depicted using PyMOL v.1.8 software (Schrödinger, LLC). Two-dimensional interaction plots were carried out with LigPlot[51].

Reporting Summary. Further information on research design is available in the Nature Research Reporting Summary linked to this article.

Data availability

The data that support the findings of this study are available from the corresponding authors upon reasonable request. Source data are provided with this paper.

References

40. Suh, B. C., Inoue, T., Meyer, T. & Hille, B. Rapid chemically induced changes of PtdIns(4,5)P2 gate KCNQ ion channels. *Science* **314**, 1454–1457 (2006).
41. Heinig, M. & Frishman, D. STRIDE: a web server for secondary structure assignment from known atomic coordinates of proteins. *Nucleic Acids Res.* **32**, W500–W502 (2004).
42. Colell, E. A., Iserte, J. A., Simonetti, F. L. & Marino-Buslje, C. MISTIC2: comprehensive server to study coevolution in protein families. *Nucleic Acids Res.* **46**, W323–W328 (2018).
43. Finn, R. D. et al. Pfam: the protein families database. *Nucleic Acids Res.* **42**, D222–D230 (2014).
44. Yin, S. Y., Ding, F. & Dokholyan, N. V. Eris: an automated estimator of protein stability. *Nat. Methods* **4**, 466–467 (2007).
45. Kabsch, W. Automatic processing of rotation diffraction data from crystals of initially unknown symmetry and cell constants. *J. Appl. Crystallogr.* **26**, 795–800 (1993).
46. Winn, M. D. et al. Overview of the CCP4 suite and current developments. *Acta Crystallogr. Sect. D. Biol. Crystal.* **67**, 235–242 (2011).
47. Vagin, A. & Teplyakov, A. Molecular replacement with MOLREP. *Acta Crystallogr. Sect. D. Biol. Crystal.* **66**, 22–25 (2010).
48. Emsley, P., Lohkamp, B., Scott, W. G. & Cowtan, K. Features and development of Coot. *Acta Crystallogr. Sect. D. Biol. Crystal.* **66**, 486–501 (2010).
49. Murshudov, G. N., Vagin, A. A. & Dodson, E. J. Refinement of macromolecular structures by the maximum-likelihood method. *Acta Crystallogr. Sect. D. Biol. Crystal.* **53**, 240–255 (1997).
50. Adams, P. D. et al. PHENIX: a comprehensive Python-based system for macromolecular structure solution. *Acta Crystallogr. Sect. D. Biol. Crystal.* **66**, 213–221 (2010).
51. Laskowski, R. A. & Swindells, M. B. LigPlot+: multiple ligand-protein interaction diagrams for drug discovery. *J. Chem. Inf. Model.* **51**, 2778–2786 (2011).

Acknowledgements

We thank L. Bertozzi and S. Thompson for help with plasmid generation. We thank R. DeRose, X.Y. Zhou and Y. Nihongaki for proofreading the manuscript. We thank H. Niwa (RIKEN), N. Sakai (RIKEN) and the staff at the BL26B2 beamline (Proposal No. 20190047) of SPring-8 (Harima, Japan) and the X06DA beamline (Proposal No. 20171001) of the Swiss Light Source, Paul Scherrer Institut (Villigen, Switzerland) for their help in X-ray diffraction data collection. We acknowledge support from the National Institutes for Health (grant nos. 5R01GM123130 to T.I., and 5R01GM123247 and 1R35 GM134864 to N.V.D.), the Passan Foundation to N.V.D., the DoD DARPA (grant no. HR0011-16-C-0139 to T.I.), and the PRESTO program of the Japan Science and Technology Agency to T.U. (grant no. JPMJPR12A3) and T.I. (grant no. JPMJPR12A5) and a Grant-in-Aid for Scientific Research (B) to T.U. (grant no. 16H05089) from the Japan Society for the Promotion of Science.

Author contributions

H.D.W. and H.N. conceived the study with input from T.I. H.D.W. carried out cell experiments and conducted image analysis with help from A.K.A. M.K. purified and crystalized split proteins, and determined protein structure by X-ray crystallography. O.D. conducted rational split site analysis. T.I., H.N., T.U. and N.V.D. supervised the project. H.D.W. wrote the manuscript in consultation with T.I. and with input from M.K., T.U., O.D. and N.V.D.

Competing interests

There is an ongoing disclosure associated with the CIT tools.

Additional information

Extended data is available for this paper at https://doi.org/10.1038/s41592-020-0913-x.

Supplementary information is available for this paper at https://doi.org/10.1038/s41592-020-0913-x.

Correspondence and requests for materials should be addressed to T.U. or T.I.

Peer review information Rita Strack was the primary editor on this article and managed its editorial process and peer review in collaboration with the rest of the editorial team.

Reprints and permissions information is available at www.nature.com/reprints.

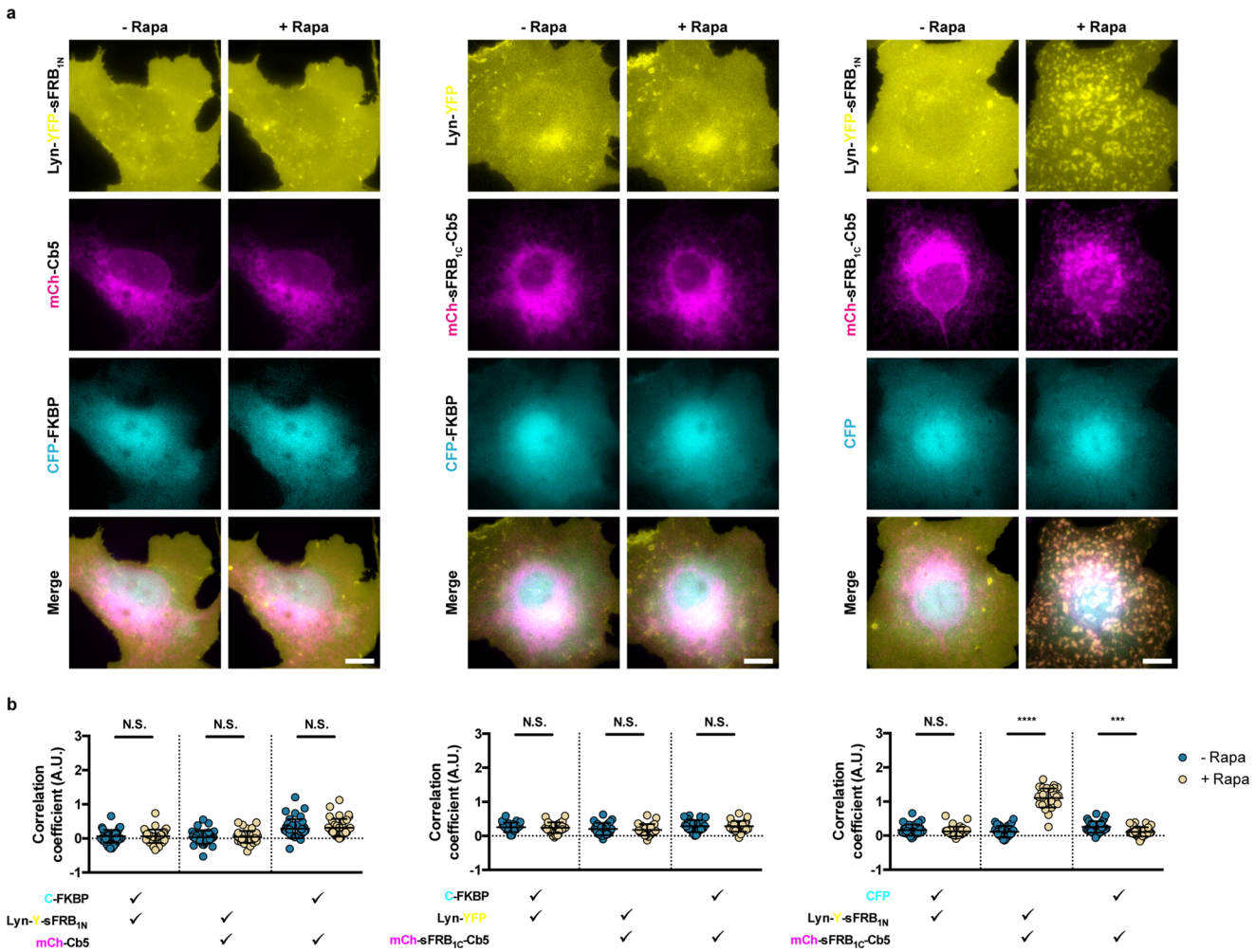

Extended Data Fig. 1 | Negative controls for cytosolic FKBP recruitment to ER-PM MCS. a, Assessing contributions of each CIT component in CFP-FKBP recruitment to ER-PM MCS; left, middle and center panels correspond to constructs lacking ER, PM, and cytosolic CIT components. **b**, Quantifying trimerization between the 3 signals pre- and post- 100 nM rapamycin. Check marks specify each combination of two wavelengths used in calculating pairwise Fisher's transformation of Pearson's correlation coefficients. Data are presented as mean values +/− SD. Two-tailed Student's t-test assuming equal variance was used to compare correlations pre- and post-rapamycin. Fom left to right: $n = 38$, 27, and 32 cells; 3 independent experiments each. Scalebar, 10 µm. (***/****; $p < 0.001/0.0001$).

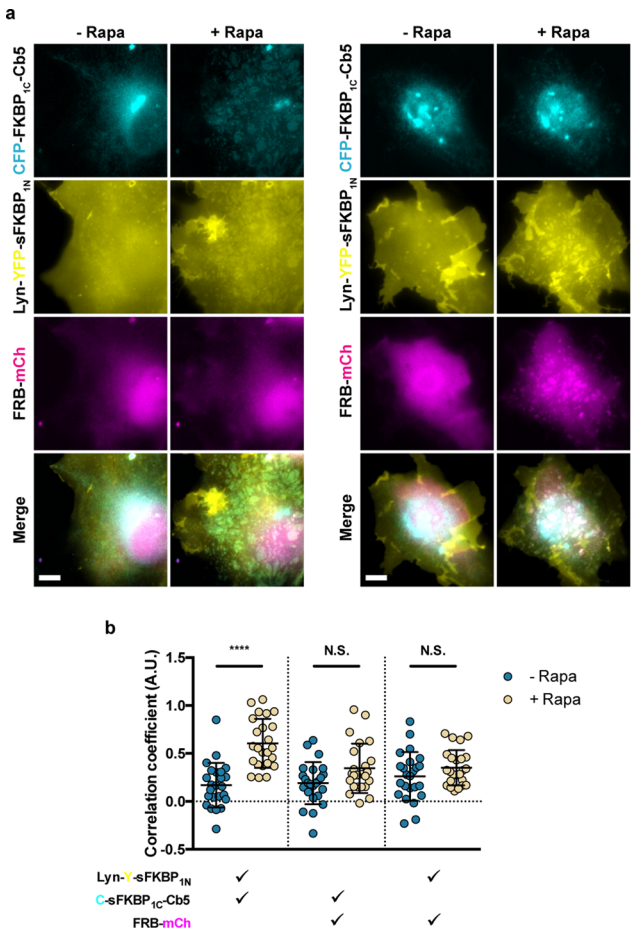

Extended Data Fig. 2 | sFKBP-based CIT recruitment of cytosolic FRB to ER-PM MCS. (**a**, **b**) Recruitment of mCh-FRB to ER-PM junctions by ER and PM targeted sFKBP1$_N$ and sFKBP$_{1C}$, pre- and 1h post- 100 nM rapamycin addition. FRB-mCh recruitment can be (a) undetectable or (b) prominent. (c) Quantifying trimerization between the 3 signals pre- and post-rapamycin. Check marks specify each combination of two wavelengths used in calculating pairwise Fisher's transformation of Pearson's correlation coefficients. Data are presented as mean values +/- SD. Two-tailed Student's t-test assuming equal variance was used to compare correlations pre- and post-rapamycin. From left to right: n = 24 cells; 3 independent experiments each. Scalebar, 10 µm. (****; $p < 0.0001$).

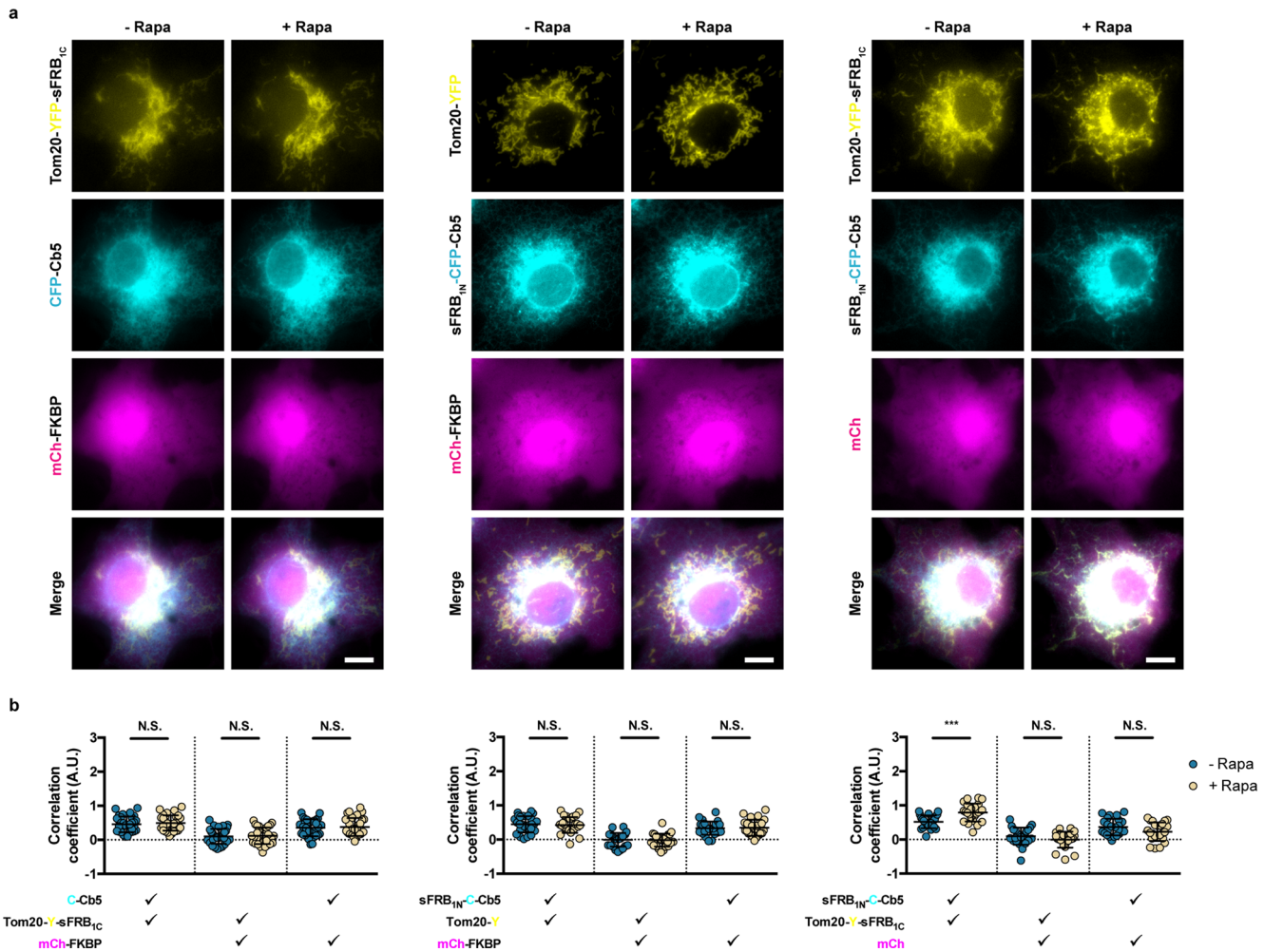

Extended Data Fig. 3 | Negative controls for cytosolic FKBP recruitment to ER-mitochondria MCS. a, Assessing contributions of each CIT component in CFP-FKBP recruitment to ER-mitochondria MCS; left, middle and center panels correspond to constructs lacking ER, mitochondria, and cytosolic CIT components. **b**, Quantifying trimerization between the 3 signals pre- and post- 100 nM rapamycin. Check marks specify each combination of two wavelengths used in calculating pairwise Fisher's transformation of Pearson's correlation coefficients. Data are presented as mean values +/− SD. Two-tailed Student's t-test assuming equal variance was used to compare correlations pre- and 12 mins post-rapamycin. From left to right: $n = 32$, 26, and 24 cells; 3 independent experiments each. Scalebar, 10 μm. (****; $p < 0.0001$).

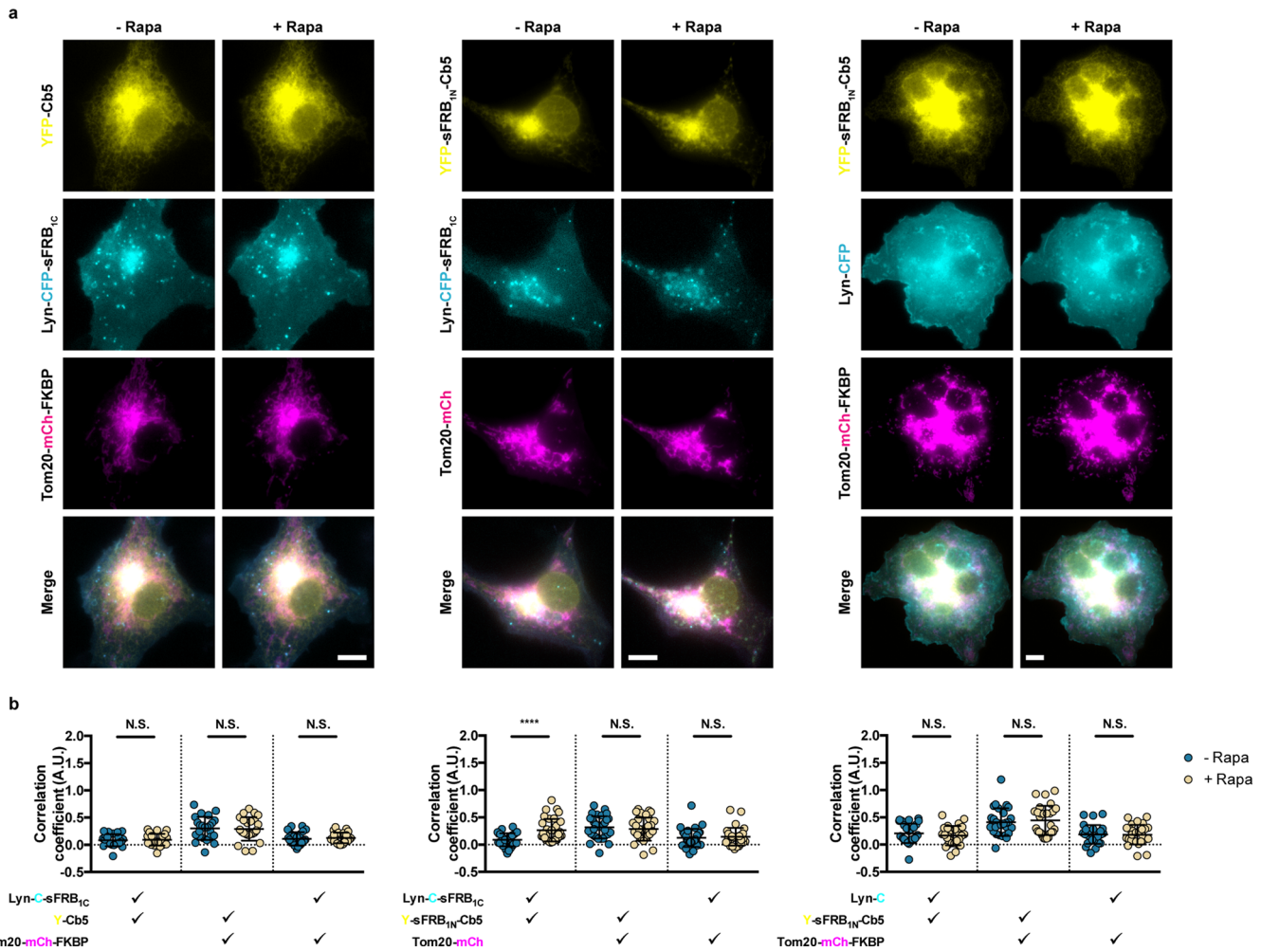

Extended Data Fig. 4 | Negative controls for CIT-induced ER-mitochondria-PM tri-organellar membrane contact sites (MCS). a, Assessing contributions of each CIT component in tri-organellar MCS formation; left, middle and center panels correspond to constructs lacking ER, mitochondria, and PM CIT components. **b**, Quantifying trimerization between the 3 signals pre- and post- 100 nM rapamycin. Check marks specify each combination of two wavelengths used in calculating pairwise Fisher's transformation of Pearson's correlation coefficients. Data are presented as mean values +/- SD. Two-tailed Student's t-test assuming equal variance was used to compare correlations pre- and 15 mins post-rapamycin. From left to right: $n = 24$, 32 and 28 cells; 3 independent experiments each. Scalebar, 10 μm. (****; $p < 0.0001$).

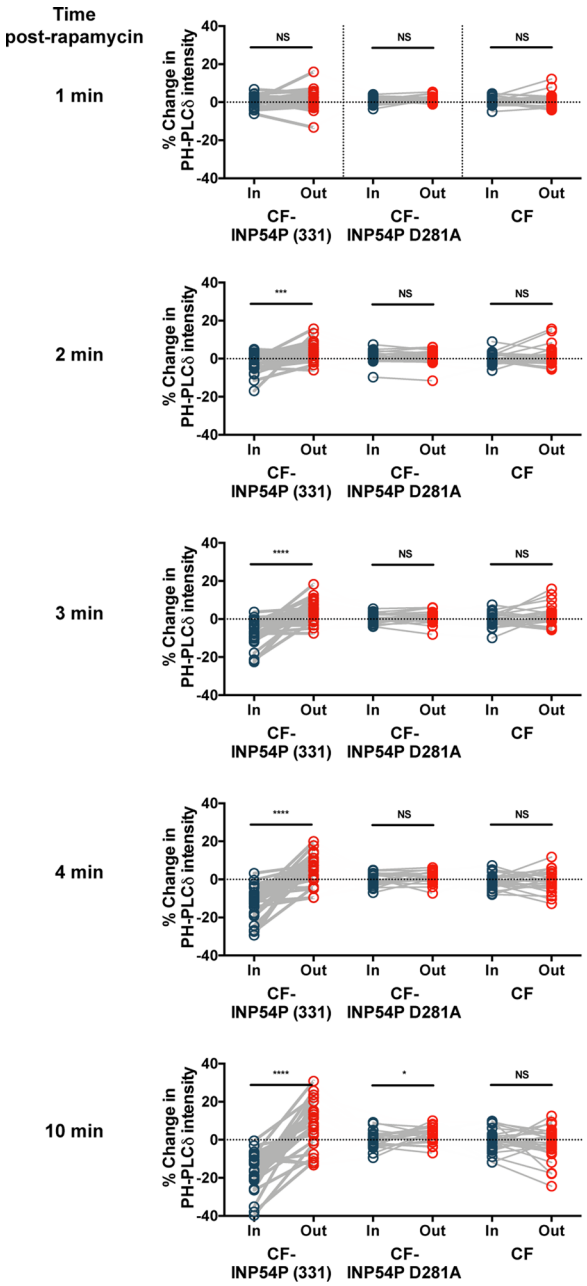

Extended Data Fig. 5 | PIP_2 biosensor intensity at ER-PM junction sites over time. Intensities of mRuby–PH-PLCδ PIP_2 biosensor of user defined regions of interest inside and outside ER-PM MCS at 1, 2, 3, 4 and 10 min after 100 nM rapamycin. Significance analyzed with two-tailed paired Students t-tests assuming equal variance. From left to right: $n = 28$, 25 and 28 cells; 4 independent experiments each. (*/***/****; $p < 0.05/0.001/0.0001$).

nature research

Corresponding author(s): Takanari Inoue

Last updated by author(s): Jun 28, 2020

Reporting Summary

Nature Research wishes to improve the reproducibility of the work that we publish. This form provides structure for consistency and transparency in reporting. For further information on Nature Research policies, see Authors & Referees and the Editorial Policy Checklist.

Statistics

For all statistical analyses, confirm that the following items are present in the figure legend, table legend, main text, or Methods section.

n/a	Confirmed	
☐	☒	The exact sample size (*n*) for each experimental group/condition, given as a discrete number and unit of measurement
☐	☒	A statement on whether measurements were taken from distinct samples or whether the same sample was measured repeatedly
☐	☒	The statistical test(s) used AND whether they are one- or two-sided *Only common tests should be described solely by name; describe more complex techniques in the Methods section.*
☒	☐	A description of all covariates tested
☒	☐	A description of any assumptions or corrections, such as tests of normality and adjustment for multiple comparisons
☐	☒	A full description of the statistical parameters including central tendency (e.g. means) or other basic estimates (e.g. regression coefficient) AND variation (e.g. standard deviation) or associated estimates of uncertainty (e.g. confidence intervals)
☐	☒	For null hypothesis testing, the test statistic (e.g. *F*, *t*, *r*) with confidence intervals, effect sizes, degrees of freedom and *P* value noted *Give P values as exact values whenever suitable.*
☒	☐	For Bayesian analysis, information on the choice of priors and Markov chain Monte Carlo settings
☒	☐	For hierarchical and complex designs, identification of the appropriate level for tests and full reporting of outcomes
☐	☒	Estimates of effect sizes (e.g. Cohen's *d*, Pearson's *r*), indicating how they were calculated

Our web collection on statistics for biologists contains articles on many of the points above.

Software and code

Policy information about availability of computer code

Data collection	Metamorph (Molecular Devices), NIS Elements (Nikon)
Data analysis	Metamorph (Molecular Devices), ImageJ Fiji (version 2.0.0-rc-69/1.52p), Microsoft Excel for Mac (version 16.16.18 (200112)), MATLAB R2016b (9.1.0.441655), PRISM 6 (Graphpad)

For manuscripts utilizing custom algorithms or software that are central to the research but not yet described in published literature, software must be made available to editors/reviewers. We strongly encourage code deposition in a community repository (e.g. GitHub). See the Nature Research guidelines for submitting code & software for further information.

Data

Policy information about availability of data

All manuscripts must include a data availability statement. This statement should provide the following information, where applicable:

- Accession codes, unique identifiers, or web links for publicly available datasets
- A list of figures that have associated raw data
- A description of any restrictions on data availability

The data that support the findings of this study are available from the corresponding authors upon reasonable request.

Field-specific reporting

Please select the one below that is the best fit for your research. If you are not sure, read the appropriate sections before making your selection.

☒ Life sciences ☐ Behavioural & social sciences ☐ Ecological, evolutionary & environmental sciences

Life sciences study design

All studies must disclose on these points even when the disclosure is negative.

Sample size	Live cell imaging: No sample size calculations were done, but sizes are consistent with current standards in the field for single-cell imaging experiments. References: doi: 10.1074/jbc.M704339200, doi: 10.1038/nmeth.1428 Positive and negative controls provided dynamic range of CID and CIT tools which also provided context for sample size. Crystallography: Multiple data sets (N ≥ 6) were collected for each structure, and a single data set with highest resolution was processed for each structure. No sample size calculations were done, but sizes are consistent with current standards in the field for X-ray crystallography.
Data exclusions	Initial screening experiments testing extent of functionality of CIT systems required seeing translocation, thus cells with sub-optimal translocation or expressing an unpromising ratio of CIT components were excluded from analysis. Exclusion criteria for each condition were established after a minimum of 3 independent experiments.
Replication	All experiments were performed in triplicate cell cultures on different days at minimum. Application of CIT was validated in HeLa and Cos-7 cells. In some cases, relative expression levels of constructs significantly affected results - not all replications were successful initially, but optimizations improved replication efficiency after a few iterations.
Randomization	No randomization was performed in order to reduce false negatives: some experimental conditions required iterative optimizations, and valuable data would have been lost during randomization.
Blinding	No blinding was conducted due to the nature of the experiments.

Reporting for specific materials, systems and methods

We require information from authors about some types of materials, experimental systems and methods used in many studies. Here, indicate whether each material, system or method listed is relevant to your study. If you are not sure if a list item applies to your research, read the appropriate section before selecting a response.

Materials & experimental systems

n/a	Involved in the study
☒	☐ Antibodies
☐	☒ Eukaryotic cell lines
☒	☐ Palaeontology
☒	☐ Animals and other organisms
☒	☐ Human research participants
☒	☐ Clinical data

Methods

n/a	Involved in the study
☒	☐ ChIP-seq
☒	☐ Flow cytometry
☒	☐ MRI-based neuroimaging

Eukaryotic cell lines

Policy information about cell lines

Cell line source(s)	HeLa (CCL2) from ATCC. Cos-7 (CRL-1651) from ATCC.
Authentication	No further authentication was done for cell lines.
Mycoplasma contamination	Beyond initial tests for mycoplasma contamination which were negative, cell lines were not tested for the rest of the experiments and data collection.
Commonly misidentified lines (See ICLAC register)	No commonly misidentified lines.